Title

Modeling Climate Change Impacts on an Arctic Polygonal Tundra: 2. Changes in CO2 and CH4 Exchange Depend on Rates of Permafrost Thaw as Affected by Changes in Vegetation and Drainage

Journal

Journal of Geophysical Research Biogeosciences, 124(5)

ISSN

2169-8953

Authors

Grant, RF
Mekonnen, ZA
Riley, WJ
et al.

Publication Date

2019-05-01

DOI

10.1029/2018jg004645

Peer reviewed

Modeling Climate Change Impacts on an Arctic Polygonal Tundra: 2. Changes in CO_2 and CH_4 Exchange Depend on Rates of Permafrost Thaw as Affected by Changes in Vegetation and Drainage

R. F. Grant[1], Z. A. Mekonnen[2], W. J. Riley[2], B. Arora[2], and M. S. Torn[2]

[1] Department of Renewable Resources, University of Alberta, Edmonton, Canada, [2] Earth Science Division, Lawrence Berkeley National Laboratory, Berkeley, CA, USA

Correspondence to: R. F. Grant, rgrant@ualberta.ca

Abstract

Model projections of future CO_2 and CH_4 exchange in Arctic tundra diverge widely. Here we used *ecosys* to examine how climate change will affect CO_2 and CH_4 exchange in troughs, rims, and centers of a coastal polygonal tundra landscape at Barrow, AK. The model was shown to simulate diurnal and seasonal variation in CO_2 and CH_4 fluxes associated with those in air and soil temperatures (T_a and T_s) and soil water contents (θ) under current climate in 2014 and 2015. During RCP 8.5 climate change from 2015 to 2085, rising T_a, atmospheric CO_2 concentrations (C_a), and precipitation (P) increased net primary productivity (NPP) from 50–150 g C m^{-2} y^{-1}, consistent with current biometric estimates, to 200–250 g C m^{-2} y^{-1}. Concurrent increases in heterotrophic respiration (R_h) were slightly smaller, so that net CO_2 exchange rose from values of −25 (net emission) to +50 (net uptake) g C m^{-2} y^{-1} to ones of −10 to +65 g C m^{-2} y^{-1}. Increases in net CO_2 uptake were largely offset by increases in CH_4 emissions from 0–6 to 1–20 g C m^{-2} y^{-1}, reducing gains in net ecosystem productivity. These increases in net CO_2 uptake and CH_4 emissions were modeled with hydrological boundary conditions that were assumed not to change with climate. Both these increases were smaller if boundary conditions were gradually altered to increase landscape drainage during model runs with climate change.

1 Introduction

A significant quantity of the large terrestrial permafrost carbon pool is thought to be vulnerable to emission as greenhouse gases (GHG) as permafrost thaw deepens with climate warming projected during this century (Schuur et al., 2015). These emissions are of particular concern in Arctic regions because the response of soil respiration to warming is greater in colder climates than in warmer (Carey et al., 2016). Most of this increased emission will be as CO_2 but some will be as CH_4, depending on changes in hydrology during climate change.

These emissions may be offset by increases in plant CO_2 uptake stimulated by rising air and soil temperatures (T_a and T_s), atmospheric CO_2 concentrations (C_a), and by more rapid soil nutrient mineralization driven by permafrost thaw and consequent increases in active layer depths (ALD;

Mauritz et al., 2017). However, increases in CO_2 uptake at high latitude sites may be seasonal, with increases in spring and early summer when radiation is less limiting and T_s and, hence, heterotrophic respiration (R_h) are low, offset by decreases in late summer and autumn when radiation is more limiting and T_s and R_h are relatively high (Mekonnen et al., 2018; Piao et al., 2008).

Some indication of how CO_2 exchange will be affected by warming has been inferred from experimental observations. Recent natural warming has been found to increase density and alter composition of tundra vegetation (e.g., Elmendorf et al., 2012), suggesting increases in net primary productivity (NPP). In a meta-analysis of experimental warming effects, Lu et al. (2013) found that increases in NPP were largely offset by increases in heterotrophic respiration (R_h) so that changes in net ecosystem productivity (NEP) were insignificant, although there was large variation among individual warming experiments. These increases in NPP were mostly attributed to increases in net N mineralization rates with soil warming.

Although changes in net CO_2 exchange with climate warming are uncertain, emissions of CH_4 are generally thought to increase. A large increase with soil warming was found in a meta-analysis of CH_4 emissions measured at research sites in different climate zones across the Arctic by Olefeldt et al. (2013). This increase may be particularly large in Alaskan wetlands, where higher water tables caused by increases in precipitation (P) or permafrost thaw and increases in graminoid abundance (Mauritz et al., 2017) will raise CH_4 emissions more than will soil warming alone (Turetsky et al., 2008).

Projections of climate change effects on net CO_2 and CH_4 exchange in Arctic regions by land surface models have given contrasting results (e.g., McGuire et al., 2018). During 100 years of rises in T_a and C_a similar to those in the RCP 8.5 emission scenario, Zhu et al. (2013) modeled increases in pan-Arctic NPP that exceeded those in R_h and, hence, modeled increases in net CO_2 uptake of 75%, as well as in CH_4 emissions of 60%. These increases were associated with increasing ALD and decreasing water table depths (WTD). However, under a similar climate change scenario, Lawrence et al. (2015) modeled increases NPP that were much smaller than those in R_h and, hence, modeled increases in net CO_2 emissions as well as only limited increases in CH_4 emissions. These increases were attributed to soil drying caused by increased drainage from permafrost thaw. The contrasting results in these two modeling studies indicate the importance of changes in subsurface hydrology in determining climate change effects on GHG exchange.

Ecosystem models used to project climate change impacts on Arctic GHG exchange must therefore explicitly and comprehensively represent processes governing changes in T_s, ALD, WTD, and consequent changes in hydrology, microbial respiration, nutrient cycling, primary productivity, and plant community composition under specified climate change scenarios. In most earlier studies (e.g., McGuire et al., 2018), many of these processes,

particularly those coupling C with N, were either not represented or represented only to a limited extent. These processes are much more comprehensively represented from basic theory in the ecosystem model *ecosys*, as described in earlier studies simulating topographic effects on changes in hydrology and ALD (Grant, Mekonnen, Riley, Wainwright, et al., 2017) and in CO_2 and CH_4 exchange (Grant, Mekonnen, Riley, Arora, et al., 2017) at the Barrow Experimental Observatory (BEO) as affected by interannual variation in temperature and precipitation under current climate (1981–2015). In both studies, model results were tested against field data recorded in different landscape features (troughs, rims, and centers) at BEO in the Next Generation Ecosystem Experiment–Arctic.

Building on these earlier studies, we present model projections from 2016 to 2085 under a RCP8.5 emission scenario of changes in CO_2 and CH_4 exchange (this paper) through those on soil water content (θ), T_s, and ALD (companion paper) in an Arctic polygonal landscape at BEO. We hypothesize that effects of climate change on CO_2 and CH_4 exchange will be determined by evolving interactions among ecosystem hydrology and biogeochemical cycling in these landscape features as climate change progresses:

1. NPP will increase with rising T_a, C_a, T_s, and consequently more rapid soil nutrient mineralization, particularly NPP of dominant graminoid PFTs.
2. Increases in aerobic R_h with rising T_s will be constrained by O_2 uptake from soil wetting caused by rising P, particularly in lower features.
3. Constraints on O_2 uptake by aerobic heterotrophs in (2) will increase anaerobic R_h with rising T_s, causing rises in CH_4 emission, particularly where growth of dominant graminoid PFTs has increased.
4. Increases in anaerobic R_h in (3) will not offset O_2 constraints on increases in aerobic R_h in (2), so that total R_h will increase more slowly than will NPP in (1).
5. NEP (= NPP − R_h) will therefore increase with climate change, particularly in lower features.
6. However, if permafrost thaw hastens subsurface drainage and thereby reduces soil wetting, O_2 constraints on aerobic R_h in (2) will be alleviated, reducing CH_4 emissions in (3) but increasing total R_h in (4) and thereby reducing NEP in (5), particularly in lower features.

2 Model Description

Ecosys is an hourly time step model with multiple canopy and soil layers that provide a framework for multispecific plant and microbial populations to acquire, transform, and exchange resources (energy, water, C, N, and P). The model is constructed from algorithms representing basic physical, chemical, and biological processes that determine process rates in plant and microbial populations interacting within complex biomes. These algorithms interact to simulate complex ecosystem behavior across a wide range of spatial scales

from square meter to continental. The model is designed to represent terrestrial ecosystems under a wide range of natural and anthropogenic disturbances and environmental changes at patch (spatially homogenous one dimensional) and landscape (spatially variable two or three dimensional) scales.

Key model equations and their parameterizations used to test the hypotheses in this study are described in Texts S1 to S8 in the supporting information to this article and summarized in Table 1 of Grant et al. (2019). These equations are cited in square brackets with regard to key model processes in the Results section below. Reference to these equations in the supporting information is intended to provide insight into model behavior but is not required to understand model results. Of particular relevance to this study are equations for energy-driven kinetics of microbial oxidation–reduction reactions that drive R_h in S1: *Microbial C, N, and P Transformations* and S8: *Inorganic N Transformations* required in hypotheses (1) and (2) above and those driving CH_4 production and consumption in S7: *CH_4 Production and Consumption* required in hypotheses (2), (3), and (4). These kinetics are first-order functions of the biomasses of heterotrophic microbial functional types (MFTs), the growths of which are driven by the energy yields of the oxidation–reduction reactions that each MFT conducts. These MFTs include obligate aerobes (bacteria and fungi) [H2–H5], facultative anaerobes (denitrifiers) [H6–H10], obligate anaerobes (fermenters) [G1–G6], heterotrophic (acetotrophic) [G7–G11] and autotrophic (hydrogenotrophic) [G12–G17] methanogens, aerobic and anaerobic heterotrophic diazotrophs (nonsymbiotic N_2 fixers) [A27–A29], and aerobic autotrophic nitrifiers [H11–H21] (Grant, 1994). The rate of decomposition also depends on the substrate concentration [A3, A5], soil temperature (T_s) (Arrhenius function) [A6], and θ [A4] (Grant et al., 2007; Grant & Rochette, 1994).

All reactants and products of these reactions are coupled to algorithms for vertical and lateral convective-diffusive transfer in gaseous and aqueous phases in S4: *Soil Water, Heat, Gas, and Solute Fluxes* required to test O_2 effects in hypothesis (2) and drainage effects in hypothesis (6). Biological processes driving primary productivity and plant growth are given in S3: *Gross Primary Productivity, Autotrophic Respiration, Growth, and Litterfall* required for *NPP* in hypothesis (1). These processes are further described in earlier modeling of CO_2 and CH_4 fluxes in tropical (Mezbahuddin et al., 2014), temperate (Dimitrov et al., 2011; Grant et al., 2012), boreal (Dimitrov et al., 2014; Grant et al., 2009; Grant & Roulet, 2002), and Arctic (Grant et al., 2015; Grant, Mekonnen, Riley, Wainwright, et al., 2017; Grant, Mekonnen, Riley, Arora, & Torn, 2017) wetlands. All parameters in these algorithms are unchanged from those in these earlier studies.

3 Site Description

The BEO is located ~6 km east of Barrow, AK (71.3°N, 156.5°W), at the northern tip of Alaska's Arctic coastal plain. Barrow has a maritime climate

characterized by long, dry winters and short, moist, cool summers, with a mean annual air temperature of −12 °C and mean annual precipitation of 106 mm. Continuous ice-rich permafrost extends to >400 m depth, overlain by a shallow active layer whose depth varies spatially and interannually from approximately 20 to 60 cm. The BEO is more fully described in Dafflon et al. (2016, 2017), Vaughn et al. (2016), and Wainwright et al. (2015).

4 Model Experiment

4.1 Model Spin-Up

4.1.1 Model Initialization

We defined the ecosys computational domains from the polygon classification scheme of Wainwright et al. (2015), in which polygons of 5–20 m at BEO were resolved into different types based on surface elevations. The low-centered polygonal (LCP) landform was represented as a center 6 m in width and length, surrounded by a rim 1 m in width and 0.2 m in height above the center, which was surrounded in turn by a trough 1 m in width and 0.2 m in depth below the rim (Figure 1a in Grant et al., 2019). The trough and the center were connected through a 1 m breach in the rim, based on the observation of Dafflon et al. (2017) that LCP ridges are variable in height. The flat-centered polygonal (FCP) landform was represented by features with the same dimensions, but the center was level with the rim (Figure 1b in Grant et al., 2019). The landform surfaces were thus 36% centers, 28% rims, and 36% troughs, similar to those derived from a high-resolution digital elevation model by Kumar et al. (2016). Other landforms such as high-centered polygons were not represented at this stage of model testing, based on the findings of Wainwright et al. (2015) that 47% of the BEO landscape is occupied by FCPs, and most of the remainder by LCPs.

Soil profiles representing the key properties of the centers, rims, and troughs used in *ecosys* are given in Table 2 of Grant, Mekonnen, Riley, Wainwright, et al., 2017. Measurements of these properties indicated greater variation within than among features with no consistent topographic effects on soil horizonation (Kumar et al., 2016). Therefore, soil properties in each feature were assumed to be the same at any depth relative to its surface so that differences in modeled hydrological and thermal conditions among features could be attributed solely to microtopographic effects.

4.1.2 Model Boundary Conditions

Surface boundary conditions were set to allow overland flow of excess surface water from troughs at the northern and southern boundaries of the modeled polygons. Snow movement across external surface boundaries was not modeled. Overland movement of water and snow among features within each landform was modeled from higher to lower topographic positions. Subsurface boundary conditions were set to allow lateral discharge and recharge of water driven by elevation differences between water tables in the boundary troughs and an external water table set to a depth of 0.025 m

below and a distance of 2.5 m from the trough surfaces at the northern and southern boundaries of the modeled polygons [D10] (Figure 1 in Grant et al., 2019). This placement of the external water table near the troughs was suggested by observations that troughs often serve as pathways for water movement through polygonal landscapes (Liljedahl et al., 2012; Woo & Guan, 2006). The WTD in each grid cell was that at which the difference between precipitation and ET from the surface energy balance within the grid cell equilibrated with the difference between discharge to and recharge from adjacent grid cells [D7] for internal grid cells and with the difference between discharge to and recharge from the external water table for boundary grid cells. An upward geothermal flux of 57 mW/m^2 was maintained across the lower boundary of the soil profile from a source assumed to be 10 m below the soil surface (Sclater et al., 1980).

Each grid cell in the LCP and FCP was initialized with the same populations of sedge (200 m^{-2}) and moss (10^4 m^{-2}) in the model year 1980. Both model polygons were run from 1980 to 2015 using gap-filled ½ hourly meteorological data (shortwave and longwave radiation, air temperature, relative humidity, windspeed, and precipitation) from 1 January 1981 to 15 June 2013 derived by Xu and Yuan (2016) from the Barrow, AK station of NOAA/Earth System Laboratory, Global Monitoring Division (http://www.esrl.noaa.gov/gmd/obop/brw/), and NOAA's National Climate Data Center, and then using 1 hourly meteorological data recorded from 16 June 2013 to 31 December 2015 at BEO by Hinzman et al. (2016). Atmospheric NH_3 concentration driving dry N deposition [D15] was set to 0.5 nmol/mol (Wentworth et al., 2016) and precipitation NH_4^+ and NO_3^- concentrations driving wet deposition were both set to 0.1 g N m^{-3} based on N deposition maps from the National Atmospheric Deposition Program. Results from these runs were presented in Grant, Mekonnen, Riley, Wainwright, et al., 2017 and Grant, Mekonnen, Riley, Arora, & Torn, 2017.

4.2 Model Runs

The model spin-up described in section 4.1 was extended through two additional 35 year cycles from model dates 1 January 2016 to 31 December 2085. These extended runs were conducted under the following meteorological boundary conditions to attribute climate change effects on ALD to increases in T_a, C_a, P, and drainage in polygonal tundra:

1. *Baseline*. Meteorological data in both cycles remained unchanged from those recorded from 1981 to 2015 (section 4.1), and atmospheric CO_2 concentration (C_a) was maintained at its 2015 value to ascertain that model results remained stable for the 70-year duration of the run. Stability would be achieved if results during the second 35-year cycle remained the same as those during the first.
2. $+T_a$. Values of T_a in (1) were incremented hourly by the increases in maximum and minimum T_a derived under RCP 8.5 emission scenario downscaled and averaged across 15 CMIP5 models for the grid cell in

which BEO is located (Table 2 in Grant et al., 2019). Relative humidity (RH) in (1) was assumed to remain constant, so that atmospheric vapor pressures (e_a) rose with T_a.

3. $+T_a + C_a$. Meteorological data in (2) were used with C_a incremented hourly by the increases expected under RCP 8.5 emission scenario (Table 2 in Grant et al., 2019).
4. $+T_a + C_a + P$ *(full climate change)*. Meteorological data and C_a in (3) were incremented hourly by the increases in P derived under RCP 8.5 emission scenario (Table 2 in Grant et al., 2019).
5. $+T_a + C_a + P + 1$. (4) was rerun with the depth of the external water table (section 4.1.2) lowered by 1 cm after every 10 years. Lowering the external water table increased discharge from, and reduced recharge to, boundary grid cells and thereby gradually increased WTD throughout the modeled landform during the run. This increase was modeled to project climate change effects on soil water content and thereby on ALD under gradual increases in drainage of polygonal tundra
6. $+T_a \pm C_a \pm P \pm 2$. (4) was rerun with the depth of the external water table (section 4.1.2) lowered by 2 cm after every 10 years to project climate change effects on soil wetting and ALD under more rapid increases in drainage of polygonal tundra.

In all runs with $+T_a$, acclimation was modeled by gradually shifting the Arrhenius functions used to simulate the temperature sensitivities of all biological processes contributing to GPP [C10a-e], R_a [C22a,b], and R_h [A6, A19] to the right by 0.3 °C for each 1 °C of warming as described in an earlier modeling study (Figure 1 in Grant, 2015).

4.3 Model Tests

4.3.1 Artificial Soil Heating Experiment

The sensitivity of modeled CO_2 fluxes to soil warming was investigated by simulating an artificial soil heating experiment conducted at BEO in which a 1.4 amp heating rod was installed vertically to a depth of 50 cm within a 30 cm diameter polyvinyl chloride (PVC) collar installed to a depth of 35 cm in a center of a high-centered polygon. Power through the heating rod was adjusted to maintain T_s averaged from 10 to 35 cm depth at 4 °C above those in a control plot from June to October in 2015. This experiment was simulated by running *ecosys* during 2015 of the FCP spin-up run with energy added each hour to all soil layers in the upper 50 cm of a center grid cell to maintain a 4 °C increase in T_s from 1 June to 31 October relative to those of the same grid cell in a control run (Figure 2b in Grant et al., 2019). Lateral movements of heat and water between the heated and adjacent grid cells were disabled to the depth of the PVC collars (35 cm).

4.3.2 Next Generation Ecosystem Experiment-Arctic

Results from the baseline run for CO_2 and CH_4 fluxes modeled during model years 2084 and 2085 under weather years 2014 and 2015 of the second weather cycle were tested with eddy covariance (EC) measurements of CO_2 fluxes by Dengel et al. (2017) in 2015 and CH_4 fluxes by Zona et al. (2015) in 2014 at BEO. For comparison with EC fluxes, model results were aggregated for all features in both the LCP and FCP (section 4.1.1) which formed the majority of the landscape within the EC fetch at BEO. Testing was conducted by evaluating intercepts (a), slopes (b), correlations (R^2), and root-mean-square for differences (RMSD) from regressions of measured on modeled fluxes, representing variation in measured values not explained by the model. A successful test was indicated by values of a near zero, b near one ($1.1 > b > 0.9$), R^2 greater than that at $p = 0.001$, and RMSD similar to root-mean-square for error representing uncertainty in measured values, indicating limited opportunity for improving agreement between modeled and measured values.

5 Results

5.1 Effects of Artificial Soil Heating on Soil CO_2 Fluxes

Artificial soil heating raised T_s modeled and measured through the upper 50 cm of the soil profile by 4 °C (Figure 2b in Grant et al., 2019), driving more rapid evaporation (Figure 3a in Grant et al., 2019) and so reducing θ relative to that of unheated control (Figure 2c in Grant et al., 2019). In the model, higher T_s raised below-ground R_a more than GPP, reducing NPP (Table 1). Higher T_s also raised R_h, causing the modeled FCP center to change from a C sink to a C source, with a loss in soil litter of 66 g C m^{-2} only partially offset by a gain in soil humus C of 5 g C m^{-2}. Higher T_s did not raise modeled CH_4 emissions in spite of greater R_h because lower θ allowed greater increases in O_2 influxes than in CO_2 effluxes (increased respiratory quotient in Table 1) [D16,D17] that increased methanotropy [G18] relative to methanogenesis [G7, G12].

Table 1

Annual Net Primary Productivity (NPP), Heterotrophic Respiration (R_h), Net CO_2 Exchange, Methane Flux (CH_4), Net Ecosystem Productivity (NEP), and Respiratory Quotient (RQ in Mole O_2 Influx/Mole CO_2 Efflux) Modeled in Control and Warmed (+4 °C From June Through October) FCP Centers During 2015 at Barrow, AK

	Control		Warmed	
	Sedge	Moss	Sedge	Moss
	g C m^{-2} y^{-1}			
GPP	152	163	151	168
R_a: above	−27	−28	−26	−28
: below	−38	−38	−45	−47
NPP	87	97	80	93
R_h:	−151		−199	
Net CO_2[a]	+34		−26	
CH_4	−0.6		−0.7	
NEP	33		−27	
RQ	0.95		0.99	

Note. Positive values represent influxes, negative values effluxes.
[a]Includes net DOC and DIC fluxes and changes in DIC stocks.

Increases in R_h and below-ground R_a drove increases in CO_2 effluxes modeled with 4 °C heating that were similar to those measured, except during August when sharp declines in effluxes measured from the unheated soil were not modeled (Figure 1a). These modeled increases were greatest during the first month of heating and then declined with depletion of the most labile litter products until the unheated soil started to freeze in September (Figure 2b in Grant et al., 2019), after which greater CO_2 effluxes persisted in the heated soil. During the warming period (June–October), 4 °C warming raised total CO_2 effluxes in the model by 36%, corresponding to a Q_{10} of 2.2. However, warming had little effect on modeled or measured CH_4 effluxes which remained small during the measurement period (Figure 1b) as θ in the heated FCP centers remained well below saturated values (Figure 2c in Grant et al., 2019). However, heating caused larger CH_4 effluxes to be modeled during earlier spring thaw before measurements began.

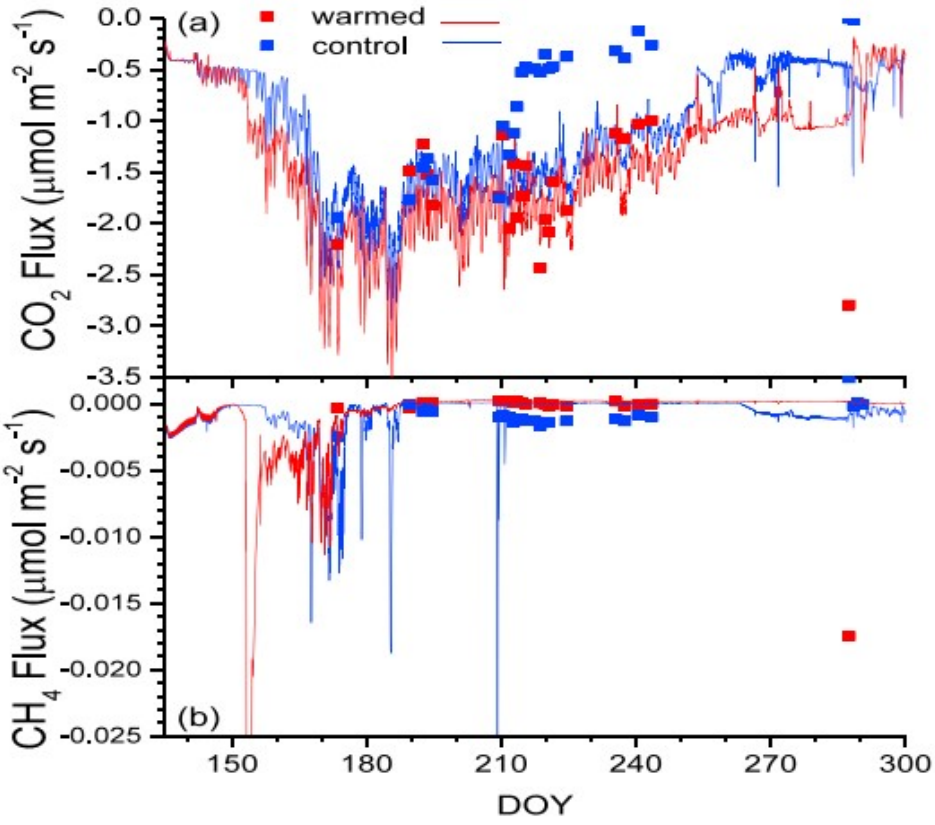

Figure 1. (a) CO_2 and (b) CH_4 fluxes measured (symbols) and modelled (lines) in control and warmed (+4°C) FCP centers during 2015 at BEO. DOY = day of year.

5.2 Model Results From Baseline Run

5.2.1 CO_2 and CH_4 Fluxes

Seasonal variation of modeled CO_2 exchange was tested against EC measurements during periods with similar T_a in late June and early September 2015 (Figure 2a). Modeled and measured CO_2 influxes were greater, and CO_2 effluxes smaller, with longer days and shallower ALD in June (Figure 5 in Grant et al., 2019) than with shorter days and deeper ALD in September (Figure 2b), indicating substantial reductions in NEP during the later growing season. Regressions of CO_2 fluxes measured during 2014 and 2015 on those modeled during 2084 and 2085 with 2014 and 2015 weather in the baseline run indicated similar biases toward larger modeled values (b < 1; Table 2) with lower R^2 (0.4–0.5) than those from earlier model tests in nonpolygonal Arctic wetlands (e.g., 0.7–0.8 in Grant et al., 2015). However, RMSD representing variation in measured fluxes not explained by the model was comparable to root-mean-square for error of the measured fluxes (Billesbach, 2011), indicating limited opportunity to improve agreement between modeled and measured fluxes.

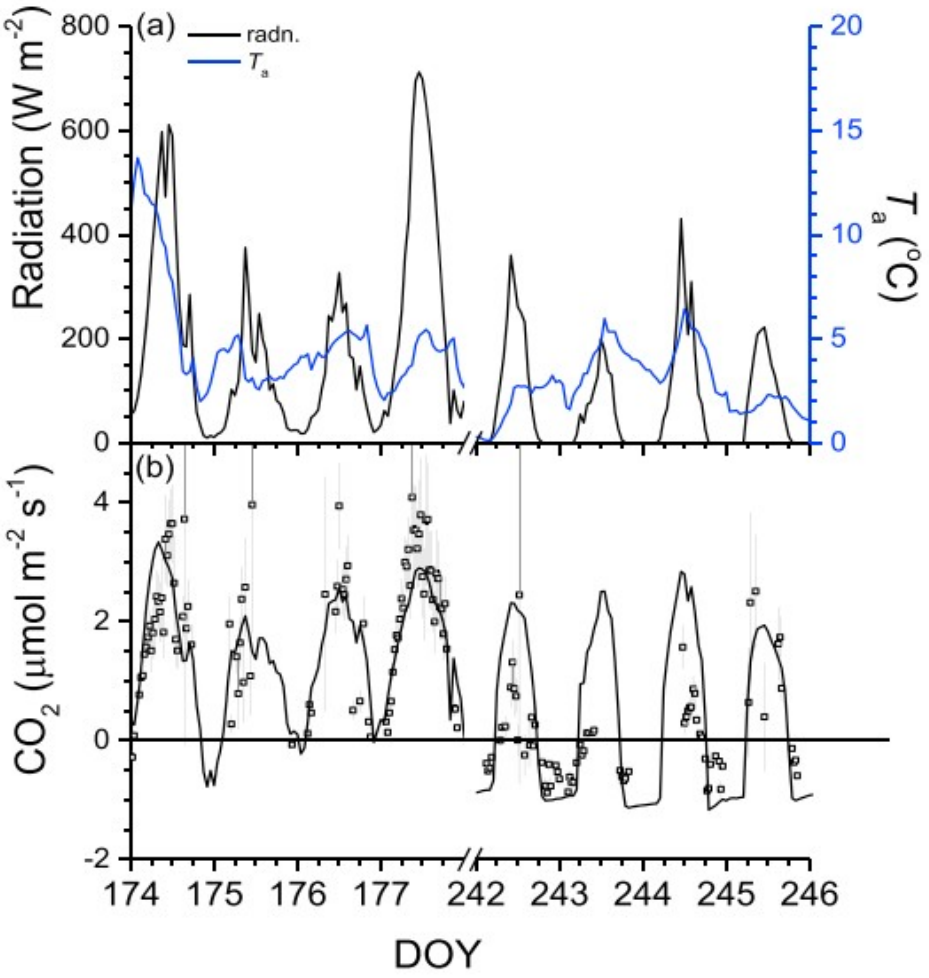

Figure 2. (a) Radiation and air temperature (T_a) and (b) CO_2 fluxes measured by eddy covariance during late June (DOY 175–178) and early September (DOY 243–246) 2015 (symbols) and spatially aggregated CO_2 fluxes modelled in combined LCP and FCP features during the same periods with 2015 weather in 2085 of the baseline run (line). In (b) positive values represent influxes, and negative values effluxes. Measured fluxes from Dengel et al. (2017). DOY = day of year; LCP = low-centered polygonal; FCP = flat-centered polygonal.

Table 2

Statistics From Regressions of Hourly Averaged CO_2 Fluxes Measured by Dengel et al. (2017) and Hourly Averaged CH_4 Fluxes Measured by Zona et al. (2015) on Those Modeled Over Combined LCP and FCP at BEO in 2014 and 2015

Year	Flux	a[a]	b[a]	R^2	RMSD[b]	RMSE	n
2014	CO_2	0.19	0.83	0.41[c]	1.34	1.57	1029
2015	CO_2	0.24	0.78	0.55[c]	1.14	1.04	721
2014	CH_4	−0.001	0.88	0.47[c]	0.006		4000

[a]$Y = a + bX$ from regression of measured Y on simulated X. [b]RMSD from regression of measured Y on simulated X. [c]Significant at $p < <0.001$.

Effluxes of CH_4 measured at BEO during 2014 by Zona et al. (2015) and modeled during 2084 with 2014 weather in the baseline run (Figure 3a) remained small during winter but rose sharply with early summer warming (DOY 170–190; Figure 3b). Effluxes declined gradually with autumn cooling (after DOY 260), sustained by shrinking active layers that persisted until the end of the year (Figure 5a in Grant et al., 2019). Large spatial variation in CH_4 effluxes modeled among landscape features was partially apparent in differences between effluxes aggregated from LCP and FCP, with respectively larger and smaller proportions of lower features. Regressions of CH_4 fluxes measured during 2014 on those modeled during 2084 in the baseline run indicated biases toward larger modeled values (b < 1; Table 2) most apparent during winter (Figure 3b).

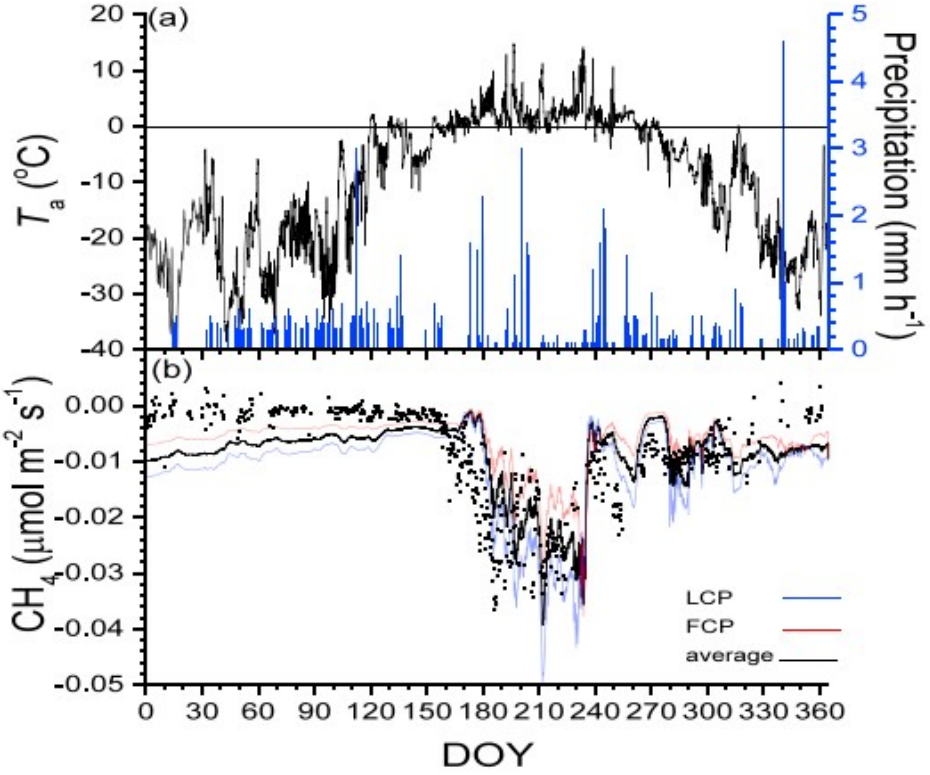

Figure 3. (a) Air temperature (T_a) and precipitation and (b) CH_4 flux measured by eddy covariance during 2014(symbols) and modelled from spatially aggregated CH_4 fluxes modelled in combined LCP and FCP features during 2084 (2014) of the baseline run (line). In (b) positive values represent influxes, and negative values effluxes. Measured fluxes from Zona et al. (2015). DOY = day of year; LCP = low-centered polygon; FCP = flat-centered polygon.

5.2.2 Annual NPP, R_h, and CH_4

The baseline run from 2016 to 2085 included two repeating 35-year weather sequences (Figures 4a, 5a, and 6a; section 4.2). Annual NPP (Figures 4b and 4c), R_h (Figures 5b and 5c), and CH_4 emissions (Figures 6b and 6c) modeled during the second sequence closely followed those during the first for all features of the LCP and FCP (b = 0.97–1.00 and R^2 = 0.98–0.99), indicating that C cycling in the model remained in equilibrium with surface boundary

conditions for the 70-year duration of the run. During both cycles, NPP and R_h of lower features remained stable, but those of higher features declined sharply during drier years and rose sharply during or following wetter years, as described in an earlier modeling study at BEO (Grant, Mekonnen, Riley, Arora, & Torn, 2017). During both cycles, CH_4 emissions from lower features rose during or following wetter years while those from higher features remained small, as described in Grant, Mekonnen, Riley, Arora, and Torn (2017).

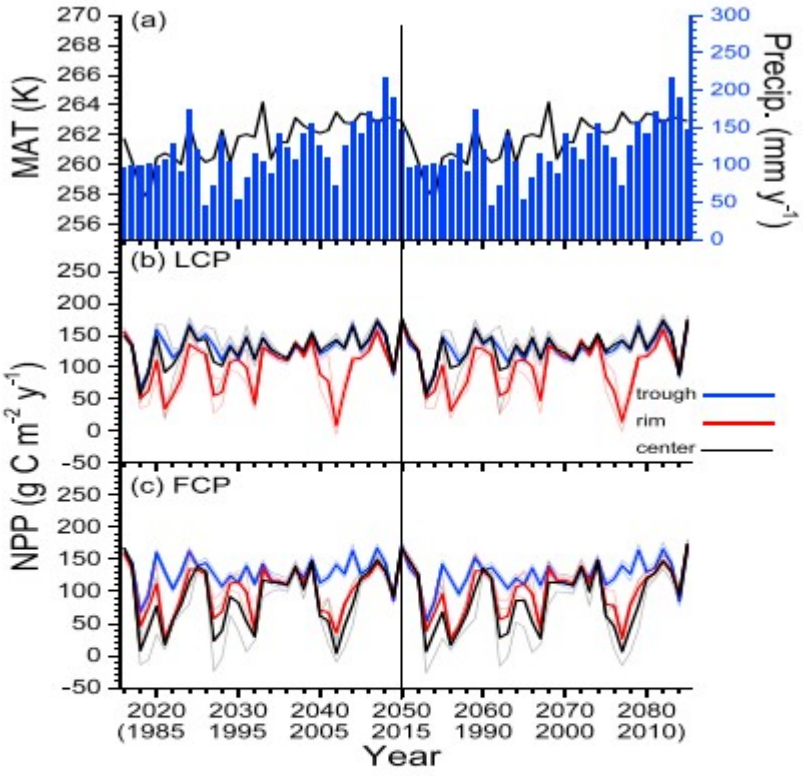

Figure 4. (a) Mean annual temperature (line) and annual precipitation (bars) at Barrow, AK, from1981 to 2015 used in the baseline run from 2016 to 2050 and from 2051 to 2085 and annual NPP modelled (lines) in troughs, rims, and centers of the (b) LCP and (c) FCP. Faint lines indicate standard deviation of values modelled for all grid cells in each feature. Meteorological data from Xu and Yuan (2016) and Hinzman et al. (2016). NPP = net primary productivity; LCP = low-centered polygon; FCP = flat-centered polygon; MAT = mean annual temperature.

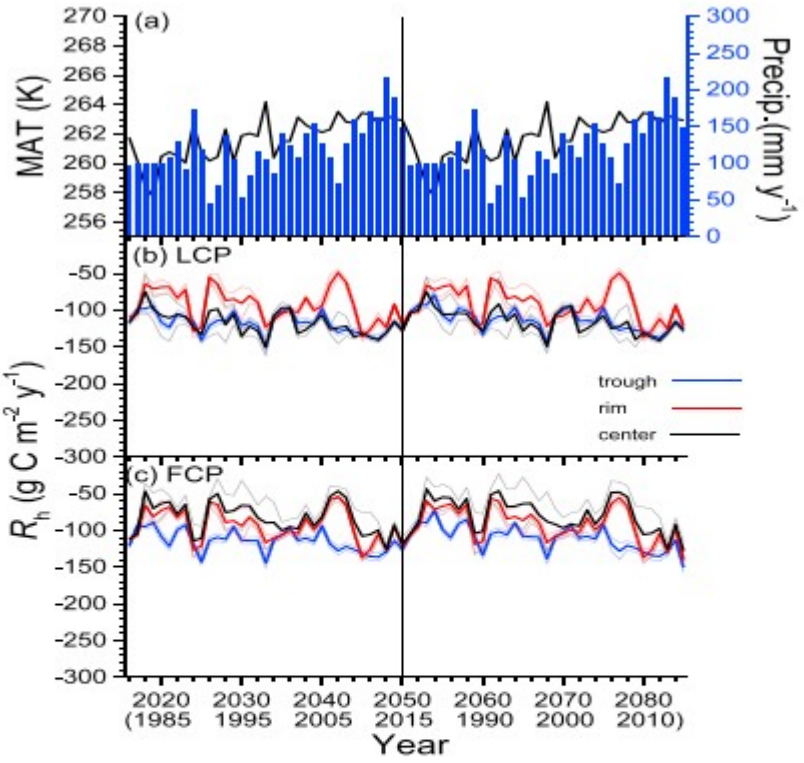

Figure 5. (a) Mean annual temperature (line) and annual precipitation (bars) at Barrow, AK, from1981 to 2015 used in the baseline run from 2016 to 2050 and from 2051 to 2085 and annual heterotrophic respiration (R_h) modelled (lines) in troughs, rims, and centers of the (b) LCP and (c) FCP. Faint lines indicate standard deviation of values modelled for all grid cells in each feature. Meteorological data from Xu and Yuan (2016) and Hinzman et al. (2016). LCP = low-centered polygon; FCP = flat-centered polygon; MAT = mean annual temperature.

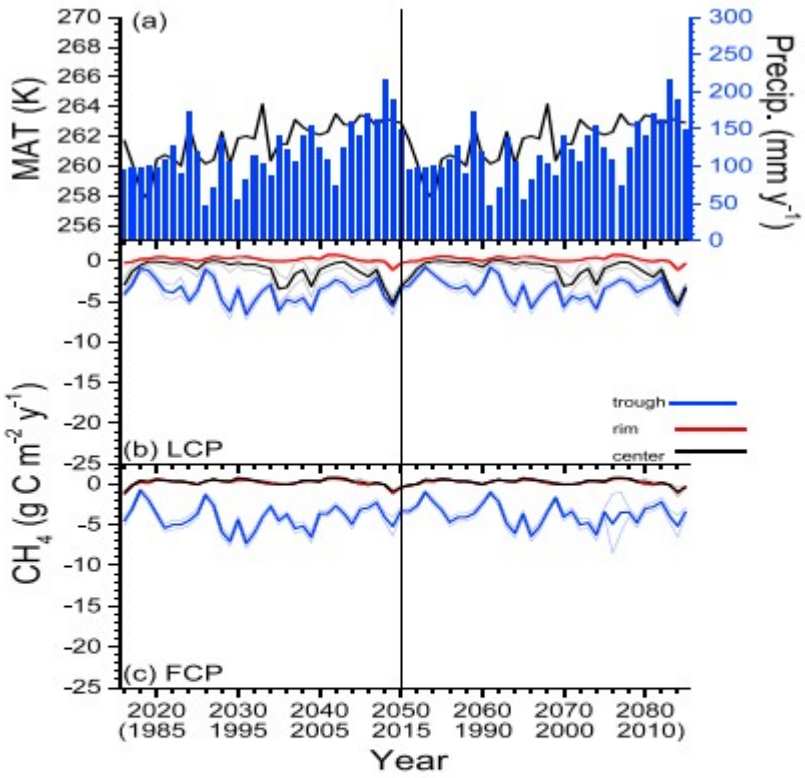

Figure 6. (a) Mean annual temperature (line) and annual precipitation (bars) at Barrow, AK, from1981 to 2015 used in the baseline run from 2016 to 2050 and from 2051 to 2085 and annual CH_4 emissions modelled in troughs, rims, and centers of the (b) LCP and (c) FCP. Faint lines indicate standard deviation of values modelled for all grid cells in each feature. Meteorological data from Xu and Yuan (2016) and Hinzman et al. (2016). LCP = low-centered polygon; FCP = flat-centered polygon; MAT = mean annual temperature.

5.3 Effects of Climate Change on Ecosystem Productivity

5.3.1 CO_2 and CH_4 Fluxes

The seasonal effects of $+T_a + C_a + P$ on ecosystem CO_2 and CH_4 fluxes were examined by comparing fluxes modeled during periods with similar T_a in late June and early September 2015 (Figure 7a) with those during the same periods after 70 years of $+T_a + C_a + P$ (Table 2 in Grant et al., 2019). CO_2 influxes increased more, and CO_2 effluxes increased less, with increased T_a in June when days were longer and ALD was shallower than in September when days were shorter and ALD was deeper (Figure 7b). These contrasting responses of CO_2 exchange to warming indicated that early season gains in NEP with climate change would be offset by late season losses. This offset was apparent in gains of daily aggregated CO_2 uptake modeled with $+T_a + C_a + P$ during spring and early summer 2085 versus losses modeled during autumn 2085 (Figure 8b). Increases in CH_4 emissions were modeled

throughout the year but were particularly large during late summer and autumn (Figures 7c and 8c).

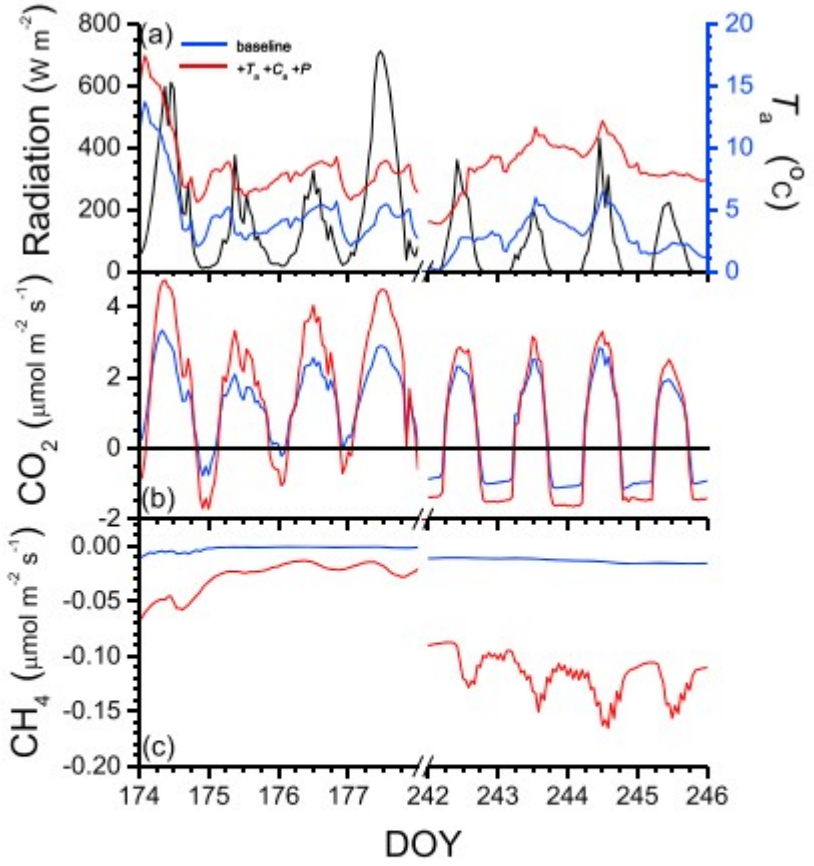

Figure 7. (a) Radiation and air temperature T_a and spatially aggregated (b) CO_2 and (c) CH_4 fluxes modelled in combined low-centered polygonal and flat-centered polygonal features during late June (DOY 175–178) and early September (DOY 243–246) 2085 in the baseline and climate change ($+T_a + C_a + P$) runs. In (b) and (c) positive values represent influxes and negative values effluxes. DOY = day of year.

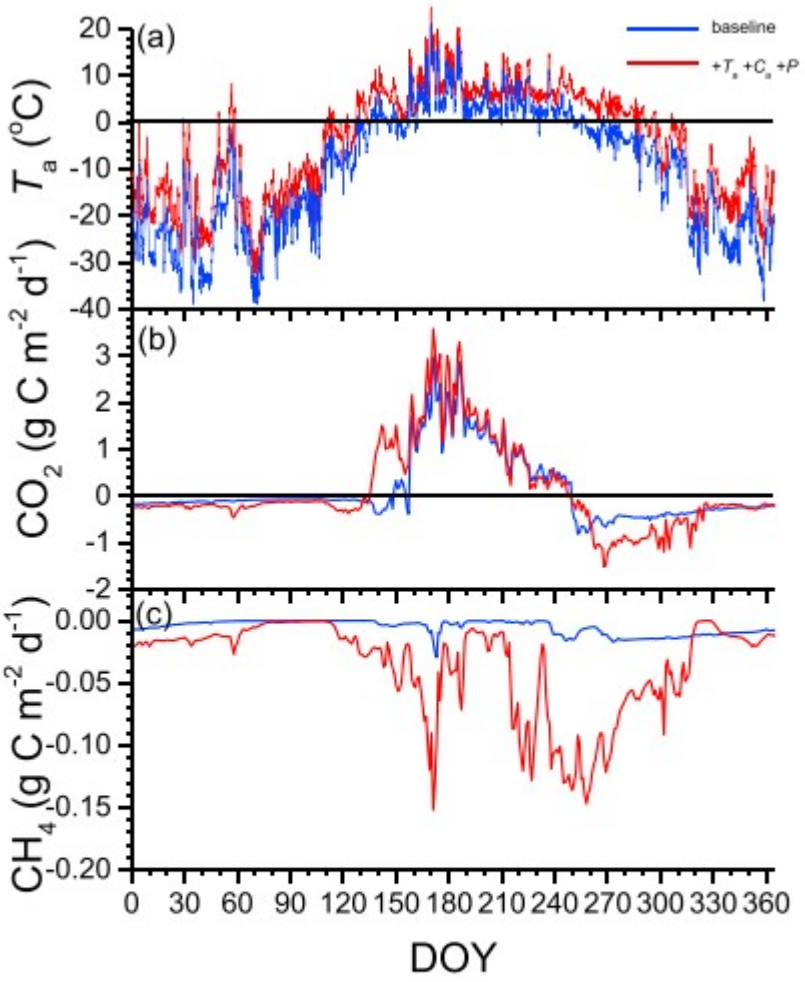

Figure 8. (a) Air temperature (T_a), precipitation, spatially aggregated daily (b) CO_2, and (c) CH_4 fluxes modelled in combined low centered and flat centered polygonal features during 2085 of the baseline and climate change ($+T_a + C_a + P$) runs. In (b) and (c) positive values represent influxes and negative values effluxes. DOY = day of year.

Changes in CO_2 exchange modeled after 70 years of $+T_a + C_a + P$ drove increases in annual NPP that were greater in higher versus lower features and in sedge versus moss (Table 3b vs. Table 3a). These increases were sustained by increases in net N mineralization [A26] and in symbiotic [F12] and nonsymbiotic [A27] N_2 fixation, driven by greater microbial growth in warmer soils with greater litterfall C inputs. Increases in sedge and moss NPP drove increases in sedge and moss LAI that altered ecosystem energy exchange, slowing rises in T_s and ET, and thereby increasing θ with $+T_a + C_a + P$ (Grant et al., 2019).

Table 3

Annual Net Primary Productivity (NPP), Heterotrophic Respiration (R_h), Net CO_2 Exchange, Methane Flux (CH_4), Net Ecosystem Productivity (NEP), and Respiratory Quotient (RQ in Mole O_2 Influx/Mole CO_2 Efflux) Modeled in Troughs, Rims, and Centers of Low- and Flat-Centered Polygons (LCP and FCP) During 2085 (2015) of the a Baseline and $b + T_a + C_a + P$ Runs at Barrow, AK

		Trough		Rim		Center	
		Sedge	Moss	Sedge	Moss	Sedge	Moss
(a) Base		g C m^{-2} y^{-}					
LCP	NPP	85	91	79	92	89	92
	R_h:	−130		−118		−131	
	Net CO_2[a]	46		51		50	
	CH_4	−3.6		−0.2		−3.4	
	NEP	42		51		46	
	RQ	0.95		0.99		0.94	
		g N m^{-2} y^{-1}					
	N_2 Fixation[b]	0.37		0.46		0.37	
	Net N Mineralization	1.15		1.21		1.24	
FCP	NPP	85	94	81	101	74	91
	R_h	−132		−126		−110	
	Net CO_2[a]	47		56		55	
	CH_4	−3.8		−0.5		−0.2	
	NEP	43		55		55	
	RQ	0.94		0.99		1.00	
		g N m^{-2} y^{-1}					
	N_2 Fixation[b]	0.36		0.53		0.46	
	Net N Mineralization	1.21		1.36		1.19	
(b) + T_a + C_a + P							
LCP	NPP	157	106	174	120	155	109
	R_h:	−209		−244		−210	
	Net CO_2 [a]	52		48		53	
	CH_4	−17.4		−8.0		−17.2	
	NEP	35		40		36	
	RQ	0.88		0.93		0.88	
		g N m^{-2} y^{-1}					
	N_2 Fixation[b]	0.50		0.68		0.54	
	Net N Mineralization	1.37		1.52		1.36	
FCP	NPP	155	110	176	132	161	121
	R_h	−211		−257		−238	
	Net CO_2[a]	53		49		42	
	CH_4	−20.2		−10.8		−8.2	
	NEP	33		38		34	
	RQ	0.87		0.92		0.93	
		g N m^{-2} y^{-1}					
	N_2 Fixation[b]	0.53		0.79		0.66	
	Net N Mineralization	1.42		1.51		1.43	

Note. Positive values represent downward fluxes, negative values upward.
[a]Includes net DIC fluxes and changes in DIC stocks. [b]Sum of symbiotic fixation by cyanobacteria in moss and non-symbiotic fixation by diazotrophic bacteria in soil.

5.3.2 Annual NPP, R_h, and CH_4

Changes in CO_2 and CH_4 fluxes modeled after 70 years of $+T_a + C_a + P$ (Figures 7 and 8) drove increases in annual R_h that largely offset those in annual NPP so that annual net CO_2 exchange rose slightly in lower features and declined slightly in higher (Table 3b vs. 3a). Increases in R_h were greater in higher than in lower features where higher θ with $+T_a + C_a + P$ caused smaller increases in O_2 uptake relative to those in CO_2 emissions, apparent as lower respiratory quotients (RQ in Table 3). Lower RQ indicated greater O_2 limitations to aerobic R_h and, hence, greater anaerobic R_h, products from which drove greater increases in CH_4 emissions from lower features than from higher (Table 3b vs. 3a).

Changes in ecosystem C exchange modeled with $+T_a + C_a + P$ developed gradually from 2016 to 2085 with increases in T_a, C_a, and P incremented over two cycles of 1981–2015 weather (Figure 9a). Annual NPP modeled in LCP and FCP features (Figures 9b and 9c) and R_h (Figures 10b and 10c) increased with mean annual air temperature (MAT_a) and P. Increases in NPP and R_h were greater in higher versus lower features (as shown for 2085 in Table 3) due to greater increases in ALD of higher features (Grant et al., 2019) from increasing P (Grant et al., 2019). Increases in NPP exceeded those in R_h modeled in all features during most years, causing net CO_2 uptake to rise as climate change progressed (Figure 11 and Table 3). Comparisons of NPP modeled with $+ T_a$, $+ T_a + C_a$ and $+ T_a + C_a + P$ indicated that effects of $+T_a + C_a + P$ on NPP were mostly determined by $+T_a$ with limited further contributions by $+C_a$ and $+ P$ (data not shown).

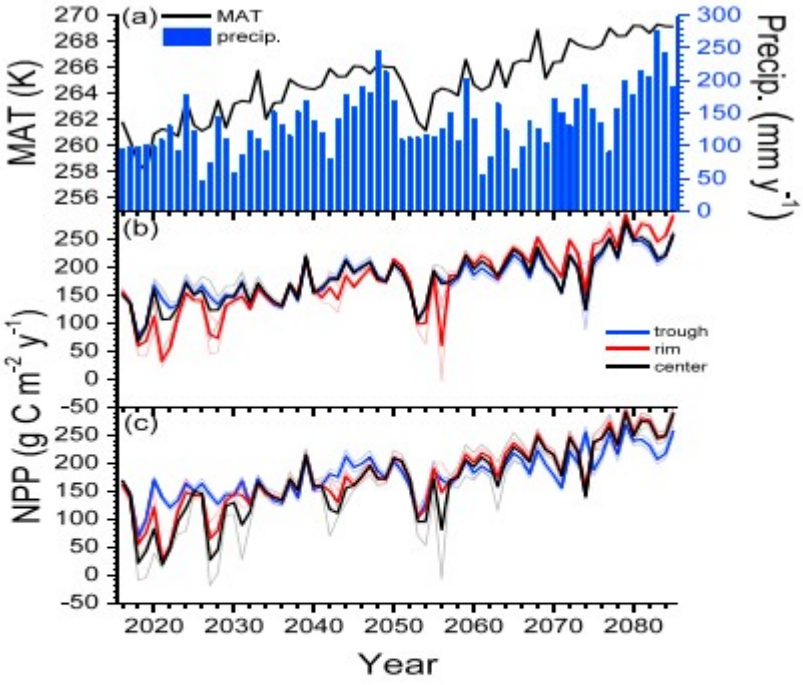

Figure 9. (a) Mean annual temperature (line) and annual precipitation (bars) at Barrow, AK, with meteorological data from 1981 to 2015 incremented hourly from 2016 to 2085 with $+ T_a + C_a + P$ (see Table 2 in Grant et al., 2019) and annual NPP modelled (lines) in troughs, rims, and centers of the (b) low-centered polygon and (c) flat-centered polygon. Faint lines indicate standard deviation of values modelled for all grid cells in each feature. NPP = net primary productivity; MAT = mean annual temperature.

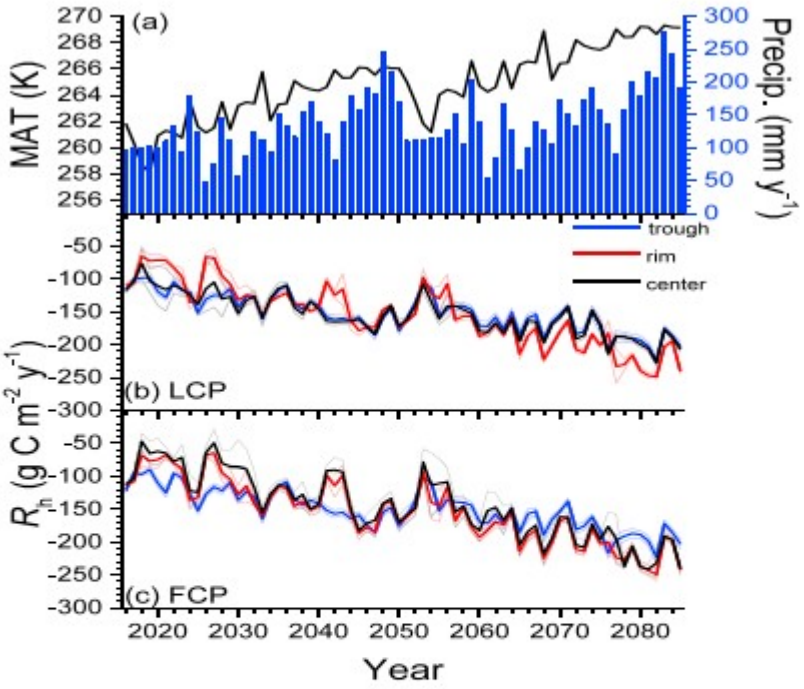

Figure 10. (a) Mean annual temperature (line) and annual precipitation (bars) at Barrow, AK, with meteorological data from 1981 to 2015 incremented hourly from 2016 to 2085 with $+ T_a + C_a + P$ (see Table 2 in Grant et al., 2019) and annual heterotrophic respiration (R_h) modelled (lines) in troughs, rims, and centers of the (b) LCP and (c) FCP. Faint lines indicate standard deviation of values modelled for all grid cells in each feature. LCP = low-centered polygon; FCP = flat-centered polygon; MAT = mean annual temperature.

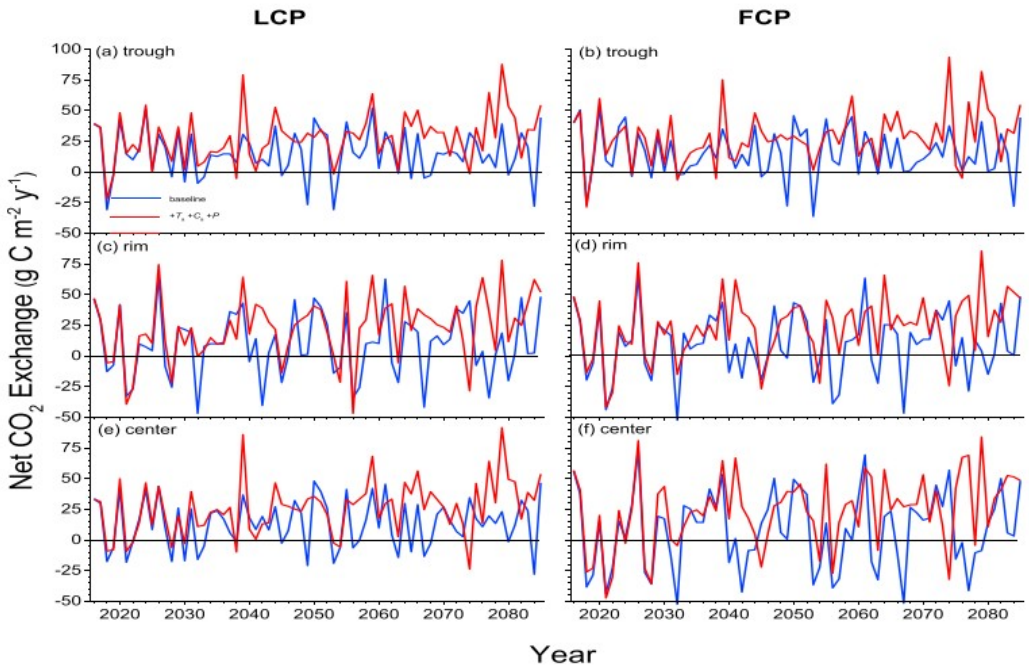

Figure 11. Annual net CO_2 exchange modelled in troughs, rims, and centers of the (a, c, and e) LCP and (b, d, and f) FCP at Barrow Experimental Observatory from 2016 to 2085 with meteorological data from 1981 to 2015 (baseline) and with these data incremented hourly with + T_a + C_a + P (see Table 2 in Grant et al., 2019). LCP = low-centered polygon; FCP = flat-centered polygon.

However, increasing O_2 limitations (lower RQ in Table 3) from increasing θ modeled with +T_a + C_a + P (Grant et al., 2019) caused sharp rises in CH_4 emissions (Figure 12 and Table 3). These rises started earlier in lower features, particularly during years with greater P, but also became apparent with wetting of higher features later in the run. Most of these rises were attributed to rising T_s from rising T_a, but increasing contributions to CH_4 emissions were attributed to rising C_a and P as climate change progressed (Figure 13). These increases reduced NEP (= net CO_2 + CH_4 exchange) during wetter years with +T_a + C_a + P (Table 3).

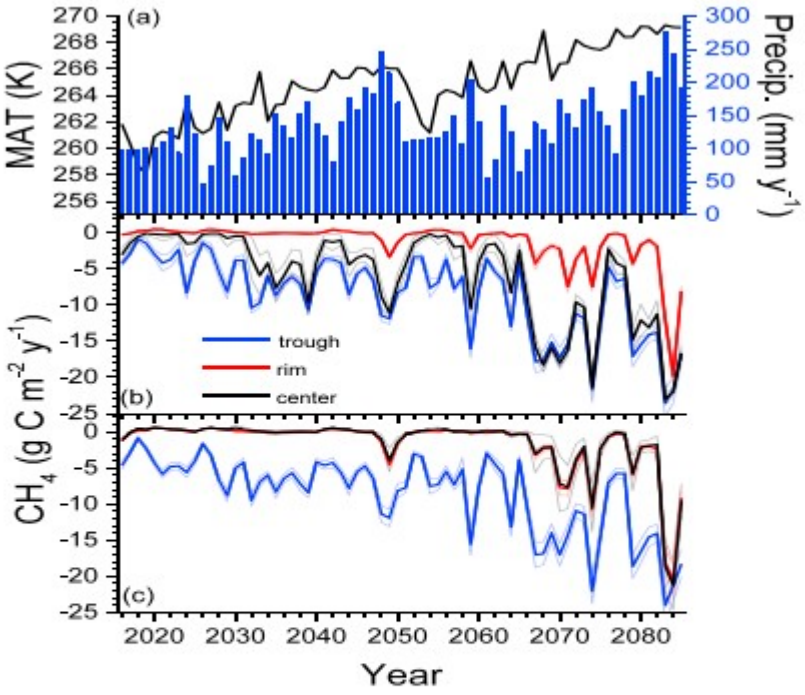

Figure 12. (a) Mean annual temperature (line) and annual precipitation (bars) at Barrow, AK, with meteorological data from 1981 to 2015 incremented hourly from 2016 to 2085 with $+ T_a + C_a + P$ (see Table 2 in Grant et al., 2019) and annual CH_4 emissions modelled in troughs, rims, and centers of the (b) low-centered polygon and (c) flat-centered polygon. Faint lines indicate standard deviation of values modelled for all grid cells in each feature. MAT = mean annual temperature.

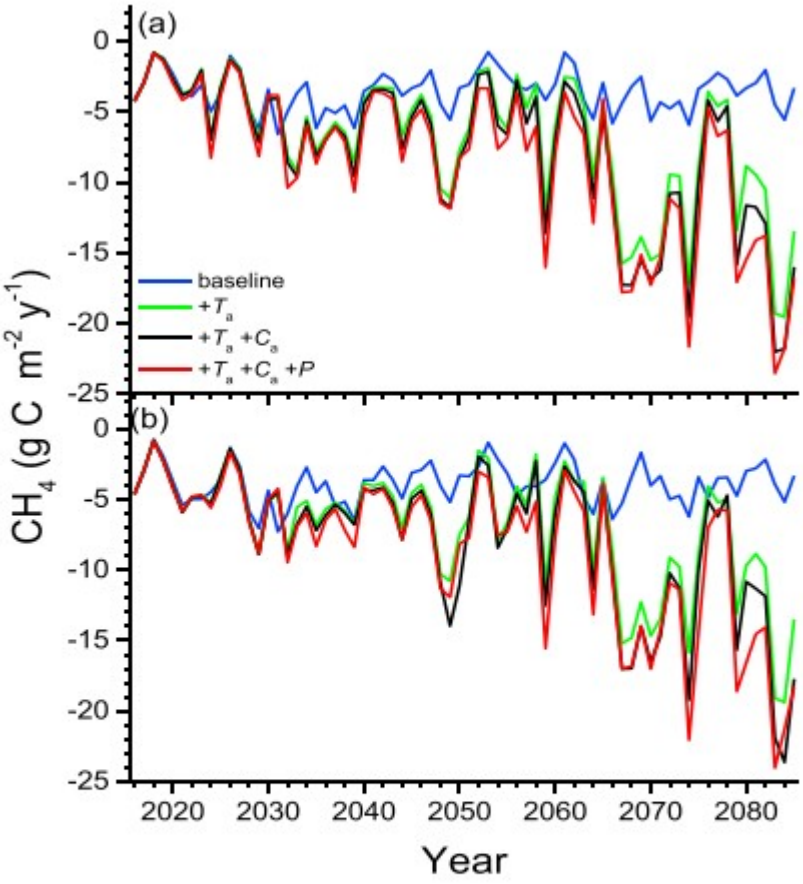

Figure 13. Annual CH_4 emissions modelled in troughs of the (a) low-centered polygon and (b) flat-centered polygon with meteorological data from 1981 to 2015 incremented hourly from 2016 to 2085 with incremented T_a (+T_a), T_a and C_a (+T_a +C_a), and T_a, C_a, and P (+ T_a + C_a + P). (see Table 2 in Grant et al., 2019).

Increases in net CO_2 uptake and CH_4 emissions modeled with +T_a + C_a + P depended upon assumptions about hydrological boundary conditions that determined landscape drainage. Improving drainage by lowering the external water table by 1 or 2 cm per decade (+T_a + C_a + P + 1 and + T_a + C_a + P + 2) had little effect on NPP in lower features but reduced NPP in higher features, particularly during drier years. Improving drainage increased R_h in lower features with rising P later in the model run but reduced R_h in higher features, particularly during drier years. Consequently, +T_a + C_a + P + 1 and + T_a + C_a + P + 2 reduced net CO_2 uptake during most years in lower and higher features (Figures 14a and 14c) as climate change progressed. Model runs with +T_a + C_a + P + 1 and + T_a + C_a + P + 2 had lower water tables (Figure 12 in Grant et al., 2019) and thereby greatly reduced CH_4 emissions in all features (Figure 15), largely offsetting reductions in net CO_2 uptake.

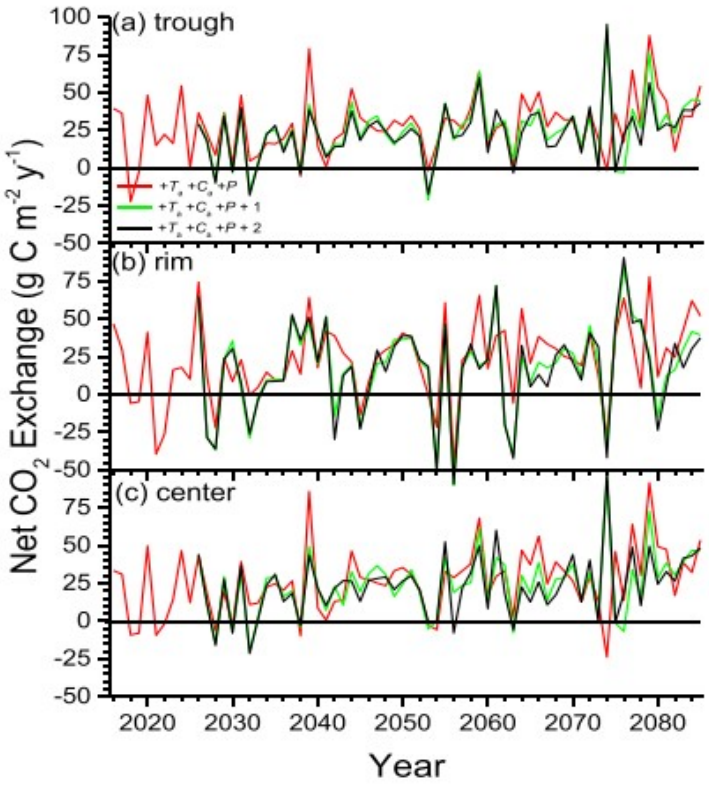

Figure 14. Annual net CO_2 exchange modelled in troughs, rims, and centers of the low-centered polygon with meteorological data from 1981 to 2015 incremented hourly with $+ T_a + C_a + P$ from 2016 to 2085 (see Table 2 in Grant et al., 2019) and with the external water table unchanged ($+ T_a + C_a + P$) or lowered by 1 ($+ T_a + C_a + P + 1$) or 2 ($+ T_a + C_a + P + 2$) cm every 10 years.

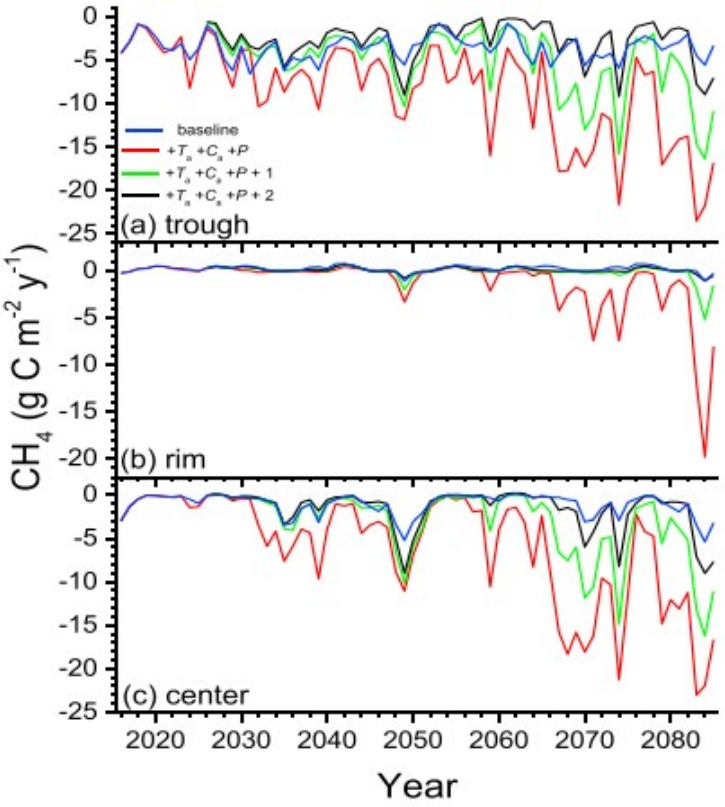

Figure 15. Annual CH_4 emissions modelled in troughs, rims, and centers of the low-centered polygon with meteorological data from 1981 to 2015 incremented hourly with + T_a + C_a + P from 2016 to 2085 (see Table 2 in Grant et al., 2019) and with the external water table unchanged (+ T_a + C_a + P) or lowered by 1 (+ T_a + C_a + P + 1) or 2 (+ T_a + C_a + P + 2) cm every 10 years.

5.3.3 Peat C and N Accumulation

During the baseline run, soil C and N accumulated at rates of 7–14 g C m^{-2} y^{-1} and 0.35–0.45 g N m^{-2} y^{-1} depending on feature elevation (Table 4a), sustained mostly by symbiotic and nonsymbiotic N_2 fixation (Table 3) and partly by wet and dry deposition (section 4.1.2). Gains in net CO_2 exchange (Figure 11) offset by losses in CH_4 emissions (Figure 12) modeled during 70 years of +T_a + C_a + P raised soil C stocks from those in the baseline run by *ca*. 450 and 800 g C m^{-2} in lower and higher features (Table 4b). These rises were sustained by gains in soil N from increases in nonsymbiotic N_2 fixation and in wet deposition from greater P. The smaller gains in soil C stocks modeled in lower features were attributed to greater C losses from cumulative CH_4 emissions. All soil gains were modeled in the upper 30 cm of the soil profile, the average ALD in the baseline run (Figure 6 in Grant et al., 2019). Very small losses of soil C were modeled below 30 cm where ALD increased with +T_a + C_a + P (Figure 9 in Grant et al., 2019) because greater C inputs from root senescence + exudation mostly offset greater C losses from R_h. Additional small gains were modeled in plant C and N stocks.

Table 4

(a) Annual Soil C and N Accumulation Rates During the 70-Year Baseline Run and (b) Changes in Soil and Plant C and N Accumulation and in Total CH_4 Emissions From Those in the Baseline Run After 70 Years of $+T_a + C_a + P$, Modeled in Troughs, Rims, and Centers of Low- and Flat-Centered Polygons (LCP and FCP)

		Soil	
		$g\ m^{-2}\ y^{-1}$	
(a) Polygon	Feature	C	N
LCP	trough	13	0.43
	rim	9	0.37
	center	14	0.43
FCP	trough	14	0.45
	rim	10	0.42
	center	7	0.35

		Soil		Plant		CH_4
		g/m^2				
(b) Polygon	Feature	C	N	C	N	
LCP	trough	433	9.7	74	1.8	345
	rim	783	11.3	209	2.3	74
	center	456	9.9	71	−0.4	339
FCP	trough	453	9.3	71	−0.4	325
	rim	812	13.1	189	2.1	96
	center	786	12.6	173	3.5	85

6 Discussion

6.1 Climate Change Impacts on Ecosystem Productivity

6.1.1 Net Primary Productivity

Greater CO_2 influxes and effluxes modeled from short-term increases in T_a with weather (Figure 2) and from long-term increases in T_a with climate (Figure 7) were largely driven by responses of GPP and R_a to increasing canopy temperatures (T_c) [C6, C14]. Arrhenius functions used to model temperature responses of GPP [C10] and R_a [C22] gave greater Q_{10} values with lower T_c and T_s (Grant, 2015), making these processes more sensitive to warming in colder climates as observed in meta-analyses of ecosystem warming experiments by Carey et al. (2016) and Lu et al. (2013).

Increases in GPP modeled with $+T_a$ were further driven by advances in onset of CO_2 fixation in spring and delays in termination of CO_2 fixation in autumn calculated from temporally integrated T_c above or below set thresholds under lengthening or shortening photoperiods, respectively. These advances and delays rose to averages of 14 days and 13 days after 70 years, extending the

growing season by 27 days (e.g., Figure 8). These predicted changes of −2 and + 2 days/dec in onset and termination of CO_2 fixation extend changes attributed to recent warming of −1.61 and 0.67 day/dec in the start and finish of photosynthetic activity from 1982 to 2014 calculated from circumpolar NDVI by Park et al. (2016).

Long-term increases in NPP with $+T_a + C_a + P$ were also driven by responses of GPP to increasing C_a [C2, C6] and in higher features to increasing P. In the baseline run, soil water deficits greatly reduced NPP modeled in higher features during drier years (Figures 4b and 4c) when low θ reduced ψ_s and increased hydraulic resistance [B9] that forced lower ψ_c [B14] and, hence, higher r_c and r_s [B2b], particularly in moss which dominated higher features (Grant, Mekonnen, Riley, Wainwright, et al., 2017). As the climate change run with $+T_a + C_a + P$ progressed, water deficit effects on NPP gradually declined (Figures 9b and 9c) with soil wetting from rises in P that exceeded those in ET. The alleviation of water deficits contributed to the greater rises in NPP modeled in higher versus lower features with $+T_a + C_a + P$ (Figures 9b and 9c).

These rises in modeled NPP were sustained from more rapid soil N mineralization [A26], and hence root N uptake [C23], driven by more rapid R_h with higher T_s (Table 3 and Figures 10b and 10c). Soil R_h and N mineralization were further hastened during climate change by increases in NPP and, hence, litterfall of sedge relative to moss (Table 3), because sedge litter had greater N content and was less recalcitrant to decomposition (Grant, Mekonnen, Riley, Arora, & Torn, 2017). The increases of net N mineralization to soil warming with $+T_a + C_a + P$ in *ecosys* (Table 3) were less than an increase of 44% in net N mineralization measured by Schaeffer et al. (2013) with summer warming of a tundra soil in Greenland by 2.4 °C, indicating that modeled increases were unlikely to have been overestimated. Rises in NPP were also sustained from more rapid N_2 fixation by microbial symbionts in moss driven by increasing moss GPP [F21–F26] (Grant et al., 2015) and by nonsymbiotic heterotrophic diazotrophs in soil [F12], driven by increasing litterfall (Table 3). The increases in symbiotic and nonsymbiotic N_2 fixation modeled under climate warming were consistent with the prediction that warmer temperatures will increase Arctic N_2 fixation rates by a factor of 1.5–2 (Chapin & Bledsoe, 1992).

Spatially averaged annual NPP modeled in the baseline run (Figures 4b and 4c) was similar to NPP from 89 to 132 g C m^{-2} y^{-1} estimated by Miller et al. (1980) from repeated biomass harvests in different wet sedge tundras at Barrow. Gains in ecosystem NPP of 50% in lower features and 70% in higher features modeled with seasonally averaged warming of 6.2 °C after 70 years of $+T_a + C_a + P$ (Figures 9b and 9c) were expected to be larger than ones of 30–40% in vascular canopy heights from a meta-analysis by Elmendorf et al. (2012) of Arctic warming experiments in which mean summer T_a was raised by an average of 1.5 °C over an average of 10 years. Gains in modeled NPP were comparable to a gain of 50% in aboveground biomass measured by

Sistla et al. (2013) after 14 years of summer warming with greenhouses in a tussock tundra. The concurrence of these modeled and measured gains indicated a strong likelihood of substantial increases in NPP of diverse Arctic ecosystems during the next century that will increase vegetative cover and thereby slow soil warming and permafrost thawing.

CO_2 uptake modeled with $+T_a + C_a + P$ (Figure 7) at BEO may be compared with that currently measured at wetland sites with warmer climates. For example, spatially aggregated GPP modeled at BEO during July 2078 rose from 82 g C m^{-2} in the baseline run with 2008 weather ($MAT_a = -10.3$ °C) to 138 g C m^{-2} with T_a and P incremented from 2008 weather ($MAT_a = -4.7$ °C). These modeled GPP were comparable with values derived from EC measurements during 2008 by Lafleur et al. (2012) of 93 ± 6 g C m^{-2} over a wet sedge tundra at Daring Lake, NWT, ($MAT_a = -10.2$ °C) and of 132 ± 7 g C m^{-2} over a wet sedge tundra at Churchill, MN, ($MAT_a = -4.9$ °C). However, Elmendorf et al. (2015) noted that inferring impacts of climate change based on spatial relationships established over much longer time scales fails to account for temporal lags in biotic responses, including migration, soil organic matter development, and other covarying biophysical limitations.

6.1.2 Heterotrophic Respiration

In the model, R_h was driven by oxidation of decomposition products mostly from aboveground and belowground litterfall but also from humus [A1] according to an Arrhenius function of T_s [A6] with the same parameters as that for R_a described above. Consequently, increases in R_h and belowground R_a modeled with artificial soil heating (Table 1) drove large increases in annual soil CO_2 effluxes (Figure 1b) that were similar to ones of 34–37% measured by Hicks Pries et al. (2017) in a similar artificial soil heating experiment in a temperate coniferous forest. The consequent loss of soil litter was consistent with observations from a meta-analysis of soil heating experiments by Lu et al. (2013).

In the model, increases in R_h with T_s hastened N_2 fixation and N and P mineralization [A26] that drove more rapid root N and P uptake [C23] that increased GPP [C6, C8] and, hence, NPP and litterfall. Increases in NPP were not modeled during the brief soil heating experiment (Table 1) but drove long-term increases in R_h over the time scales at which the different components of litterfall decomposed and mineralized (Figure 10). Consequently, increases in R_h modeled after 70 years of $+T_a + C_a + P$ were greater than those modeled in the artificial soil heating experiment, even though increases in T_s were similar (Grant et al., 2019).

Changes in R_h modeled with $+T_a + C_a + P$ differed with changes in hydrology among landscape features. Long-term climate change caused soil wetting with increased θ and reduced WTD (Figure 11 in Grant et al., 2019). In lower features with higher θ, soil wetting slowed increases in O_2 supply by gaseous convection–dispersion [D16] with smaller air-filled porosity [D17] relative to increases in O_2 demand with rising T_s [A6]. Increases in O_2 supply with soil

warming were further slowed in all features by reduced gaseous solubility that forced lower aqueous O_2 concentrations ($[O_{2s}]$) relative to gaseous O_2 concentrations during gaseous-aqueous dissolution at air-water interfaces [D14] and by increased path lengths with higher θ that slowed aqueous O_2 diffusion from air-water interfaces to aerobic microbial surfaces [A17b]. Consequent reductions in $[O_{2s}]$ at microbial surfaces slowed rises in O_2 uptake by aerobic heterotrophs [A17a] relative to rises in O_2 demand [A16] with rising T_s [A6] and increased substrate from litterfall [A1]. Slower rises in O_2 uptake slowed rises in aerobic R_h [A14] and hence in DOC uptake [A21b] relative to DOC production from decomposition [A1]. Consequent increases in DOC concentrations drove more rapid anaerobic (fermenter) R_h [G1]. However, energy yield from anaerobic R_h [G4] was smaller than that from aerobic R_h [A21a], driving slower anaerobic versus aerobic microbial growth [G6] versus [A25] that reduced rises in total R_h with soil warming in lower features as O_2 became more limiting (Table 3).

In higher features with lower θ where O_2 supply was less limiting, soil wetting increased habitat volume for microbial heterotrophs, improving access to substrate [A4] and thereby increasing R_h relative to that in lower features with higher θ. Consequently, increases in R_h modeled with soil wetting from $+T_a + C_a + P$ were greater in higher features than in lower (Figure 10).

6.1.3 Net CO_2 Exchange

The increase in R_h modeled with artificial soil heating exceeded that in GPP, causing the FCP center to change from a sink to a source of C (Table 1). This response of net CO_2 exchange modeled with rapid soil heating differed from that modeled with gradual soil warming from $+T_a + C_a + P$ in which net CO_2 uptake increased, although with large spatial and interannual variability (Table 3 and Figure 11). The contrasting responses of net CO_2 exchange to warming were attributed in the model to the limited effect on NPP from short-term (June–October) soil heating with no increase in T_a (Table 1) versus a strong increase in NPP from gradual soil warming during 70 years of $+T_a + C_a + P$ (Figure 9). These contrasting responses indicate that impacts on net CO_2 exchange of long-term climate change will likely differ from those of short-term soil heating experiments.

Modeled gains in net CO_2 uptake with $+T_a + C_a + P$ were greater in spring and early summer than in late summer (Figure 7), consistent with experimental observations by Hobbie and Chapin (1998) that warming stimulated tundra GPP during the early growing season but stimulated tundra R_e throughout the growing season. Greater net CO_2 emissions modeled with $+T_a + C_a + P$ in autumn (Figure 8) were consistent with findings from a combination of inversion modeling and a meta-analysis of EC fluxes in which losses from net CO_2 emissions in autumn offset 90% of gains from net CO_2 uptake in spring with recent warming in northern ecosystems (Piao et al., 2008). The seasonality of changes in net CO_2 exchange was also modeled by Mekonnen et al. (2018) with warming from 1980 to 2010 across

the North American Arctic using *ecosys* with the North American Regional Reanalysis meteorological data set.

Peat C and N accumulation rates driven by net CO_2 and CH_4 exchange modeled during the baseline run at BEO (Table 4a) were expected to be lower than mean rates of 23 ± 2 and 0.5 ± 0.4 g C m^{-2} y^{-1} estimated by Loisel et al. (2014) in a meta-analysis of Holocene C accumulation at sites in northern peatlands that were mostly warmer than Barrow. The gains in net CO_2 uptake modeled under $+T_a + C_a + P$ versus baseline runs (Figure 11) were consistent with findings from meta-analyses of Arctic warming experiments by Oberbauer et al. (2007) that warming of wet sedge tundra caused greater increases in GPP than in R_e which was constrained by high θ and shallow WTD. The smaller gains and greater losses in net CO_2 uptake modeled with improved drainage from $+T_a + C_a + P + 1$ and $+ T_a + C_a + P + 2$ versus $+T_a + C_a + P$ (Figure 14) were also consistent with findings by Oberbauer et al. (2007) that warming of dry tundra sites raised R_e relative to GPP, particularly when GPP was reduced at higher T_a. The consequent increases in peat C accumulation modeled with $+T_a + C_a + P$ (Table 4b) are consistent with inferences drawn from the meta-analysis of Loiset et al. (2014) that warm summers promote C sequestration based on increased accumulation rates measured during the Holocene Thermal Maximum.

However, the gains in net CO_2 uptake modeled under $+T_a + C_a + P$ in this study (Figure 11) contrasted with observations from some other studies in the Arctic that indicate a trend toward net C loss from artificial and natural warming. Mauritz et al. (2017) found that artificial soil warming increased net CO_2 emissions outside the growing season more than net CO_2 uptake during the growing season, as was modeled with artificial soil heating in this study (Table 1). Belshe et al. (2013) inferred from a meta-analysis of CO_2 flux measurements that net CO_2 emissions increased similarly to, but remained larger than, net CO_2 uptake with recent air warming in Arctic landscapes. The gains in net CO_2 uptake modeled under $+T_a + C_a + P$ in this study also contrasted with increases in net CO_2 emissions from thawing permafrost modeled with climate change in some earlier modeling studies summarized in Schaefer et al. (2014). These increases in net CO_2 emissions were not modeled in this study at BEO (Table 4) because R_h in thawing permafrost was limited by low $[O_{2s}]$ below water tables maintained above the permafrost table (Figure 11 in Grant et al., 2019).

6.2 Climate Change Impacts on CH_4 Fluxes

More rapid fermenter R_h modeled with soil warming and wetting under $+T_a + C_a + P$ (section 6.1.2) drove more rapid fermentation [G1], products of which drove more rapid acetotrophic and hydrogenotrophic methanogenesis [G7, G12]. Emissions of CH_4 from methanogenesis were further hastened by slower methanotrophy from reduced $[O_{2s}]$ [G21] and by more rapid transfer of CH_4 through a denser network of porous sedge roots [D16d] maintained by increased sedge NPP (Table 3). The combined physical and biological effects

of θ and T_s on [O_{2s}] and thereby on fermentation and methanogenesis enabled the large apparent temperature sensitivity of CH_4 emissions to be modeled with activation energies commonly used in Arrhenius functions for biological activity [A6, G1, G7, G12] (Grant, 2015). This modeled sensitivity accounts for the large apparent Q_{10} values for CH_4 emissions frequently derived from experimental studies in wetlands (e.g., Walter and Heimann (2000) and Whiting and Chanton (1993)).

The sensitivity of fermentation and methanogenesis to T_s and θ also enabled the model to simulate the large seasonal variation in CH_4 emissions measured at BEO, including nongrowing season emissions (Figure 3) sustained by ice-free zones modeled during autumn and early winter (Figure 5 in Grant et al., 2019). Annual CH_4 emissions modeled in lower features during the baseline run (Figure 6) were similar to ones from 2.7 to 6.2 g C m^{-2} y^{-1} estimated from 1999 to 2003 at Barrow from measurements by Harazono et al. (2006).

The combined physical and biological effects of θ and T_s on fermentation and methanogenesis caused the sharp rises in annual CH_4 emissions modeled in lower features with $+T_a + C_a + P$ (Figure 12), much of which was attributed to rises in T_s with $+T_a$ (Figure 13). These rises caused spatially averaged emissions to approach 150 mg C m^{-2} d^{-1} during summers (Figure 8), within the upper range of fluxes currently measured across a wide range of Arctic sites in a meta-analysis by Olefeldt et al. (2013). These large increases in CH_4 emissions are consistent with a general expectation that soil warming with associated changes in soil hydrology and increased sedge dominance will cause substantial increases in CH_4 emissions. Turetsky et al. (2008) found a strong interaction between soil warming and WTD that raised seasonal CH_4 emissions measured in an Alaskan peatland by 80–300% in response to near-surface (2 cm) warming of 0.6 °C and a reduction in WTD of 10 cm. Consequently, they projected that CH_4 emissions under climate change would be further raised by higher water tables from increases in precipitation or permafrost thaw. Comparable increases in annual CH_4 emissions modeled here during 70 years with $+T_a + C_a + P$ were driven by larger increases in near-surface T_s (2.4–3.2 °C in lower features and 2.9–4.7 °C in higher features) and a similar reduction of *ca*. 10 cm in WTD (Figure 12 in Grant et al., 2019) to those in Turetsky et al. (2008).

Increases in annual CH_4 emissions modeled with $+T_a + C_a + P$ were further driven by large increases in R_h (Figure 10) caused by increases in NPP and, hence, litterfall (Figure 9) because increases in aerobic R_h lowered [O_{2s}] and consequent increases in anaerobic R_h by fermenters generated more substrates for methanogenesis. Increases in annual CH_4 emissions modeled with $+T_a + C_a + P$ were also driven by increased CH_4 transport through root aerenchyma from increased sedge cover (Table 3; Table 5 in Grant et al., 2019) which by itself may more than double CH_4 emissions (Olefeldt et al., 2013). These increases were modeled without surface subsidence caused by warming, which is not yet simulated in *ecosys*. Annual CH_4 emissions

modeled in lower features after 70 years with $+T_a + C_a + P$ (Figure 12) ($MAT_a = -4$ °C) were similar to ones of 18–22 g C m^{-2} y^{-1} calculated from gap-filled eddy covariance measurements by Jackowicz-Korczyński et al. (2010) in a palsa mire peatland underlain by discontinuous permafrost in northern Sweden ($MAT_a = -1$ °C). Given the limited increases in net CO_2 uptake modeled with $+T_a + C_a + P$, increases in CH_4 emissions became the dominant feedback of climate change on atmospheric radiative forcing from permafrost thawing in this study.

However, increases in modeled CH_4 emissions were sensitive to assumptions about subsurface hydrology and so declined sharply with greater topographic elevation and subsurface drainage (Figure 15). Similarly, Lawrence et al. (2015) modeled large increases in CH_4 emissions with RCP 8.5 climate warming when drainage from thawed permafrost was prevented but much smaller increases when drainage was enabled. Better understanding and accurate modeling of long-term changes in landscape hydrology is therefore vital to improving confidence in projections of long-term changes in net GHG exchange.

7 Summary

1. RCP 8.5 climate change from 2015 to 2085 increased NPP from 50–150 g C m^{-2} y^{-1} under current climate, consistent with current biometric estimates, to 200–250 g C m^{-2} y^{-1} after 70 years of climate change.
2. Concurrent increases in heterotrophic respiration (R_h) were slightly smaller, so that net CO_2 exchange rose from values of −25 (net emission) to +50 (net uptake) g C m^{-2} y^{-1} under current climate to ones of −10 to +65 g C m^{-2} y^{-1} after 70 years of climate change.
3. Increases in net CO_2 uptake were largely offset by increases in CH_4 emissions from 0–6 g C m^{-2} y^{-1} under current climate to 1–20 g C m^{-2} y^{-1} after 70 years of climate change, reducing gains in NEP.
4. These increases in net CO_2 uptake and CH_4 emissions were modeled with an external WTD that was assumed not to change with climate. Both these increases were smaller if boundary conditions were gradually altered to increase landscape drainage and thereby increase WTD during model runs with climate change.

Acknowledgments

High performance computing facilities for ecosys were provided by Compute Canada (www.computecanada.ca) through the WestGrid computing network (https://www.westgrid.ca). Field research was supported by the Director, Office of Science, Office of Biological, and Environmental Research of the U.S. Department of Energy under contract DE-AC02-05CH11231 to Lawrence Berkeley National Laboratory as part of the Next-Generation. Ecosystem Experiments in the Arctic project. Data used in this paper are available from the NGEE website as cited in the text.

References

Belshe, E. F., Schuur, E. A. G., & Bolker, B. M. (2013). Tundra ecosystems observed to be CO_2 sources due to differential amplification of the carbon cycle. *Ecology Letters*, 16(10), 1307– 1315. https://doi.org/10.1111/ele.12164

Billesbach, D. P. (2011). Estimating uncertainties in individual eddy covariance flux measurements: A comparison of methods and a proposed new method. *Agricultural and Forest Meteorology*, 151(3), 394– 405. https://doi.org/10.1016/j.agrformet.2010.12.001

Carey, J. C., Tang, J., Templer, P. H., Kroeger, K. D., Crowtherd, T. W., Burton, A. J., Dukes, J. S., Emmett, B., Frey, S. D., Heskel, M. A., Jiang, L., Machmuller, M. B., Mohan, J., Panetta, A. M., Reich, P. B., Reinsch, S., Wang, X., Allison, S. D., Bamminger, C., Bridgham, S., Collins, S. L., de Dato, G., Eddy, W. C., Enquistz, B. J., Estiarte, M., Harte, J., Henderson, A., Johnson, B. R., Larsen, K. S., Luo, Y., Marhan, S., Melillo, J. M., Peñuelas, J., Pfeifer-Meister, L., Poll, C., Rastetter, E., Reinmann, A. B., Reynolds, L. L., Schmidt, I. K., Shaver, G. R., Strong, A. L., Suseela, V., & Tietema, A. (2016). Temperature response of soil respiration largely unaltered with experimental warming. *PNAS*, 113(48), 13,797– 13,802. https://doi.org/10.1073/pnas.1605365113

Chapin, D. M., & Bledsoe, C. S. (1992). Nitrogen fixation in Arctic plant communities. In F. S. Chapin, R. L. Jefferies, J. F. Reynolds, & G. R. Shaver (Eds.), *Arctic ecosystems in a changing climate: An ecophysiological perspective*, (pp. 301– 319). San Diego: Academic press.

Dafflon, B., Hubbard, S., Ulrich, C., Peterson, J., Wu, Y., Wainwright, H., & Kneafsey, T. J. (2016). Geophysical estimation of shallow permafrost distribution and properties in an ice-wedge polygon-dominated Arctic tundra region. *Geophys*, 81(1), WA247– WA263. https://doi.org/10.1190/geo2015-0175.1

Dafflon, B., Oktem, R., Peterson, J., Ulrich, C., Tran, A. P., Romanovsky, V., & Hubbard, S. S. (2017). Coincident aboveground and belowground autonomous monitoring to quantify covariability in permafrost, soil, and vegetation properties in Arctic tundra. *Journal of Geophysical Research: Biogeosciences*, 122, 1321– 1342. https://doi.org/10.1002/2016JG003724

Dengel, S., Torn, M. S., & Billesbach, D. (2017). Eddy-Covariance and auxiliary measurements, NGEE-Barrow, 2012–2016. http://ngee-arctic.ornl.gov/. accessed 21.11.2017.

Dimitrov, D. D., Bhatti, J. S. & Grant, R. F. (2014). The transition zones (ecotone) between boreal forests and peatlands: Ecological controls on ecosystem productivity along a transition zone between upland black spruce forest and a poor forested fen in central Saskatchewan. *Ecological Modelling*, 291, 96– 108.

Dimitrov, D. D., Grant, R. F., LaFleur, P. M., & Humphreys, E. (2011). Modelling the effects of hydrology on gross primary productivity and net ecosystem productivity at Mer Bleue bog. *Journal of Geophysical Research*, 116, G04010. https://doi.org/10.1029/2010JG001586

Elmendorf, S. C., Henry, G. H. R., Hollister, R. D., Björk, R. G., Bjorkman, A. D., Callaghan, T. V., Collier, L. S., Cooper, E. J., Cornelissen, J. H. C., Day, T. A., Fosaa, A. M., Gould, W. A., Grétarsdóttir, J., Harte, J., Hermanutz, L., Hik, D. S., Hofgaard, A., Jarrad, F., Jónsdóttir, I. S., Keuper, F., Klanderud, K., Klein, J. A., Koh, S., Kudo, G., Lang, S. I., Loewen, V., May, J. L., Mercado, J., Michelsen, A., Molau, U., Myers-Smith, I. H., Oberbauer, S. F., Pieper, S., Post, E., Rixen, C., Robinson, C. H., Schmidt, N. M., Shaver, G. R., Stenström, A., Tolvanen, A., Totland, Ø., Troxler, T., Wahren, C. H., Webber, P. J., Welker, J. M., & Wookey, P. A. (2012). Global assessment of experimental climate warming on tundra vegetation: Heterogeneity over space and time. *Ecology Letters*, 15(2), 164– 175. https://doi.org/10.1111/j.1461-0248.2011.01716.x

Elmendorf, S. C., Henry, G. H. R., Hollister, R. D., Fosaa, A. M., Gould, W. A., Hermanutz, L., Hofgaard, A., Jónsdóttiri, I. S., Jorgenson, J. C., Lévesque, E., Magnusson, B., Molau, U., Myers-Smith, I. H., Oberbauer, S. F., Rixen, C., Tweedieand, C. E., & Walker, M. D. (2015). Experiment, monitoring and gradient methods used to infer climate change effects on plant communities yield consistent patterns. *PNAS*, 112(2), 448– 452. https://doi.org/10.1073/pnas.1410088112

Grant, R. F. (1994). Simulation of ecological controls on nitrification. *Soil Biology and Biochemistry*, 26, 305– 315.

Grant, R. F. (2015). Ecosystem CO_2 and CH_4 exchange in a mixed tundra and a fen within a hydrologically diverse Arctic landscape. Part II. Modelled impacts of climate change. *Journal of Geophysical Research: Biogeosciences*, 120, 1388– 1406. https://doi.org/10.1002/2014JG002889

Grant, R. F., Arkebauer, T. J., Dobermann, A., Hubbard, K. G., Schimelfenig, T. T., Suyker, A. E., Verma, S. B., & Walters, D. T. (2007). Net biome productivity of irrigated and rainfed maize – soybean rotations: modelling vs. measurements. *Agronomy Journal*, 99, 1404– 1423.

Grant, R. F., Desai, A., & Sulman, B. (2012). Modelling contrasting responses of wetland productivity to changes in water table depth. *Biogeosciences*, 9, 4215– 4231.

Grant, R. F., Humphreys, E. R., & Lafleur, P. M. (2015). Ecosystem CO_2 and CH_4 exchange in a mixed tundra and a fen within a hydrologically diverse Arctic landscape. Part I. Modelling vs. measurements. *Journal of Geophysical Research: Biogeosciences*, 120, 1366– 1387. https://doi.org/10.1002/2014JG002888

Grant, R. F., Margolis, H. A., Barr, A. G., Black, T. A., Dunn, A. L., Bernier, P. Y., & Bergeron, O. (2009). Changes in net ecosystem productivity of boreal

black spruce stands in response to changes in temperature at diurnal and seasonal time scales. *Tree Physiology*, 29(1), 1– 17. https://doi.org/10.1093/treephys/tpn004

Grant, R. F., Mekonnen, Z. A., Riley, W. J., Arora, B., & Torn, M. S. (2017). Mathematical modelling of Arctic polygonal tundra with *ecosys*: 2. Microtopography determines how CO_2 and CH_4 exchange responds to changes in temperature and precipitation. *Journal of Geophysical Research: Biogeosciences*, 122, 3174– 3187. https://doi.org/10.1002/2017JG004037

Grant, R. F., Mekonnen, Z. A., & Riley W. J. (2019). Modelling climate change impacts on an Arctic polygonal tundra. Part 1: Rates of permafrost thaw depend on changes in vegetation and drainage. *Journal of Geophysical Research: Biogeosciences*, 124. https://doi.org/10.1029/2018JG004644

Grant, R. F., Mekonnen, Z. A., Riley, W. J., Wainwright, H. M., Graham, D., & Torn, M. S. (2017). Mathematical modelling of Arctic polygonal tundra with *ecosys*: 1. Microtopography determines how active layer depths respond to changes in temperature and precipitation. *Journal of Geophysical Research: Biogeosciences*, 122, 3161– 3173. https://doi.org/10.1002/2017JG004035

Grant, R. F., & Rochette, P. (1994). Soil microbial respiration at different temperatures and water potentials: Theory and mathematical modelling. *Soil Science Society of America Journal*, 58, 1681– 1690.

Grant, R. F., & Roulet, N. T. (2002). Methane efflux form boreal wetlands: Theory and testing of the ecosystem model *ecosys* with chamber and tower flux measurements. *Global Biogeochemical Cycles*, 16(4), 1054. https://doi.org/10.1029/2001GB001702

Harazono, Y., Mano, M., Miyata, A., Yoshimoto, M., Zulueta, R. C., Vourlitis, G. L., Kwon, H., & Oechel, W. C. (2006). Temporal and spatial differences of methane flux at Arctic tundra in Alaska. *Memoirs of National Institute of Polar Research*, 59, 79– 95.

Hicks Pries, C. E., Castanha, C., Porras, R., & Torn, M. S. (2017). The whole-soil carbon flux in response to warming. *Science*, 355(6332), 1420– 1423. https://doi.org/10.1126/science.aal1319

Hinzman, L., V. Romanovsky, W. Cable and G. Busey (2016), Surface meteorology, Barrow, Alaska, Area A, B, C and D, ongoing from 2012. http://ngee-arctic.ornl.gov/. accessed 19 January 2016.

Hobbie, S. E., & Chapin, F. S. III (1998). The response of tundra plant biomass, aboveground production, nitrogen, and CO_2 flux to experimental warming. *Ecology*, 79(5), 1526– 1544.

Jackowicz-Korczyński, M., Christensen, T. R., Bäckstrand, K., Crill, P., Friborg, T., Mastepanov, M., & Ström, L. (2010). Annual cycle of methane emission from a subarctic peatland. *Journal of Geophysical Research*, 115, G02009. https://doi.org/10.1029/2008JG000913

Kumar, J., Collier, N., Bisht, G., Mills, R. T., Thornton, P. E., Iversen, C. M., & Romanovsky, V. (2016). Modeling the spatiotemporal variability in subsurface thermal regimes across a low-relief polygonal tundra landscape. *The Cryosphere*, 10(5), 2241– 2274. https://doi.org/10.5194/tc-10-2241-2016

Lafleur, P. M., Humphreys, E. R., Louis, V. L. S., Myklebust, M. C., Papakyriakou, T., Poissant, L., Barker, J. D., Pilote, M., & Swystun, K. A. (2012). Variation in peak growing season net ecosystem production across the Canadian Arctic. *Environmental Science & Technology*, 46(15), 7971–7977. https://doi.org/10.1021/es300500m

Lawrence, D. M., Koven, C. D., Swenson, S. C., Riley, W. J., & Slater, A. G. (2015). Permafrost thaw and resulting soil moisture changes regulate projected high-latitude CO_2 and CH_4 emissions. *Environmental Research Letters*, 10, 094011.

Liljedahl, A. K., Hinzman, L. D. & Schulla, J. (2012). Ice-wedge polygon type controls low-gradient watershed-scale hydrology. In K. M. Hinkel (Eds.), *Tenth International Conference on Permafrost* (Vol. 1, pp. 231– 236). Salekhard, Russia: International Contributions, The Northern Publisher.

Loisel, J., Yu, Z., Beilman, D. W., Camill, P., Alm, J., Amesbury, M. J., Anderson, D., Andersson, S., Bochicchio, C., Barber, K., Belyea, L. R., Bunbury, J., Chambers, F. M., Charman, D. J., de Vleeschouwer, F., Fiałkiewicz-Kozieł, B., Finkelstein, S. A., Gałka, M., Garneau, M., Hammarlund, D., Hinchcliffe, W., Holmquist, J., Hughes, P., Jones, M. C., Klein, E. S., Kokfelt, U., Korhola, A., Kuhry, P., Lamarre, A., Lamentowicz, M., Large, D., Lavoie, M., MacDonald, G., Magnan, G., Mäkilä, M., Mallon, G., Mathijssen, P., Mauquoy, D., McCarroll, J., Moore, T. R., Nichols, J., O'Reilly, B., Oksanen, P., Packalen, M., Peteet, D., Richard, P. J. H., Robinson, S., Ronkainen, T., Rundgren, M., Sannel, A. B. K., Tarnocai, C., Thom, T., Tuittila, E. S., Turetsky, M., Väliranta, M., van der Linden, M., van Geel, B., van Bellen, S., Vitt, D., Zhao, Y., & Zhou, W. (2014). A database and synthesis of northern peatland soil properties and Holocene carbon and nitrogen accumulation. *Holocene*, 24(9), 1028– 1042. https://doi.org/10.1177/0959683614538073

Lu, M., Zhou, X., Yang, Q., Li, H., Luo, Y., Fang, C., Chen, J., Yang, X., & Li, B. (2013). Responses of ecosystem carbon cycle to experimental warming: A meta-analysis. *Ecology*, 94(3), 726– 738. https://doi.org/10.1890/12-0279.1

Mauritz, M., Bracho, R., Celis, G., Hutchings, J., Natali, S. M., Pegoraro, E., Salmon, V. G., Schädel, C., Webb, E. E., & Schuur, E. A. G. (2017). Nonlinear CO2 flux response to 7 years of experimentally induced permafrost thaw. *Global Change Biology*, 23(9), 3646– 3666. https://doi.org/10.1111/gcb.13661

McGuire, D. A., Lawrence, D. M., Koven, C., Clein, J. S., Burke, E., Chen, G., Jafarov, E., MacDougall, A. H., Marchenko, S., Nicolsky, D., Peng, S., Rinkem, A., Ciais, P., Gouttevin, I., Hayes, D. J., Ji, D., Krinner, G., Moore, J. C.,

Romanovsky, V., Schädel, C., Schaefer, K., Schuur, E. A. G., & Zhuang, Q. (2018). Dependence of the evolution of carbon dynamics in the northern permafrost region on the trajectory of climate change. *PNAS*, 115(15), 3882, 3887. https://doi.org/10.1073/pnas.1719903115

Mekonnen, Z. A., Grant, R. F., & Schwalm, C. (2018). Modelling impacts of recent warming on seasonal carbon exchange in higher latitudes of North America. *Arctic Science*, 4(4), 471– 484. https://doi.org/10.1139/as-2016-0009

Mezbahuddin, M., Grant, R. F., & Hirano, T. (2014). Modelling effects of seasonal variation in water table depth on net ecosystem CO_2 exchange of a tropical peatland. *Biogeosciences*, 11(3), 577– 599. https://doi.org/10.5194/bg-11-577-2014

Miller, P. C., Webber, P. J., Oechel, W. C., & Tieszen, L. L. (1980). Biophysical processes and primary production. In J. Brown, P. C. Miller, L. L. Tieszen, & F. L. Bunell (Eds.), *An Arctic ecosystem: The coastal tundra at Barrow, Alaska. US/IBP synthesis series 12*, (pp. 66– 101). Dowden, Stroudsberg, PA.: Hutchison and Ross, Inc.

Oberbauer, S. F., Tweedie, C. E., Welker, J. M., Fahnestock, J. T., Henry, G. H. R., Webber, P. J., Hollister, R. D., Walker, M. D., Kuchy, A., Elmore, E., & Starr, G. (2007). Tundra CO_2 fluxes in response to experimental warming across latitudinal and moisture gradients. *Ecological Monographs*, 77(2), 221– 238. https://doi.org/10.1890/06-0649

Olefeldt, D., Turetsky, M. R., Crill, P. M., & Mcguire, A. D. (2013). Environmental and physical controls on northern terrestrial methane emissions across permafrost zones. *Global Change Biology*, 19(2), 589– 603. https://doi.org/10.1111/gcb.12071

Park, T., Ganguly, S., Tømmervik, H., Euskirchen, E. S., Høgda, K.-A., Karlsen, S. R., Brovkin, V., Nemani, R. R., & Myneni, R. B. (2016). Changes in growing season duration and productivity of northern vegetation inferred from long-term remote sensing data. *Environmental Research Letters*, 11(8). https://doi.org/10.1088/1748-9326/11/8/084001

Piao, S., Ciais, P., Friedlingstein, P., Peylin, P., Reichstein, M., Luyssaert, S., Margolis, H., Fang, J., Barr, A., Chen, A., Grelle, A., Hollinger, D. Y., Laurila, T., Lindroth, A., Richardson, A. D., & Vesala, T. (2008). Net carbon dioxide losses of northern ecosystems in response to autumn warming. *Nature*, 451(7174), 49– 52. https://doi.org/10.1038/nature06444

Schaefer, K., Lantuit, H., Romanovsky, V. E., Schuur, E. A. G., & Witt, R. (2014). The impact of the permafrost carbon feedback on global climate. *Environmental Research Letters*, 9(8), 085003. https://doi.org/10.1088/1748-9326/9/8/085003

Schaeffer, S. M., Sharp, E., Schimel, J. P., & Welker, J. M. (2013). Soil–plant N processes in a high arctic ecosystem, NW Greenland are altered by long-term

experimental warming and higher rainfall. *Global Change Biology*, 19, 3529–3539. https://doi.org/10.1111/gcb.12318

Schuur, E. A. G., McGuire, A. D., Schädel, C., Grosse, G., Harden, J. W., Hayes, D. J., Hugelius, G., Koven, C. D., Kuhry, P., Lawrence, D. M., Natali, S. M., Olefeldt, D., Romanovsky, V. E., Schaefer, K., Turetsky, M. R., Treat, C. C., & Vonk, J. E. (2015). Climate change and the permafrost carbon feedback. *Nature*, 520(7546), 171– 179. https://doi.org/10.1038/nature14338

Sclater, J. G., Jaupart, C., & Galson, D. (1980). The heat flow through oceanic and continental crust and the heat loss of the Earth. *Reviews of Geophysics and Space Physics*, 18(1), 269– 311. https://doi.org/10.1029/RG018i001p00269

Sistla, S. A., Moore, J. C., Simpson, R. T., Gough, L., Shaver, G. R., & Schimel, J. P. (2013). Long-term warming restructures Arctic tundra without changing net soil carbon storage. *Nature*, 497(7451), 615– 618. https://doi.org/10.1038/nature12129

Turetsky, M. R., Treat, C. C., Waldrop, M. P., Waddington, J. M., Harden, J. W., & McGuire, A. D. (2008). Short-term response of methane fluxes and methanogen activity to water table and soil warming manipulations in an Alaskan peatland. *Journal of Geophysical Research*, 113, G00A10. https://doi.org/10.1029/2007JG000496

Vaughn, L. J. S., Conrad, M. E., Bill, M., & Torn, M. S. (2016). Isotopic insights into methane production, oxidation, and emissions in Arctic polygon tundra. *Global Change Biology*, 22(10), 3487– 3502. https://doi.org/10.1111/gcb.13281

Wainwright, H. M., Dafflon, B., Smith, L. J., Hahn, M. S., Curtis, J. B., Wu, Y., Ulrich, C., Peterson, J. E., Torn, M. S., & Hubbard, S. S. (2015). Identifying multiscale zonation and assessing the relative importance of polygon geomorphology on carbon fluxes in an Arctic tundra ecosystem. *Journal of Geophysical Research: Biogeosciences*, 120, 788– 808. https://doi.org/10.1002/2014JG002799

Walter, B. P., & Heimann, M. (2000). A process-based climate-sensitive model to derive methane emissions from natural wetlands: Application to five wetland sites, sensitivity to model parameters, and climate. *Global Biogeochemical Cycles*, 14(3), 745– 765. https://doi.org/10.1029/1999GB001204

Wentworth, G. R., Murphy, J. G., Croft, B., Martin, R. V., Pierce, J. R., Côté, J. S., Courchesne, I., Tremblay, J. É., Gagnon, J., Thomas, J. L., Sharma, S., Toom-Sauntry, D., Chivulescu, A., Levasseur, M., & Abbatt, J. P. D. (2016). Ammonia in the summertime Arctic marine boundary layer: Sources, sinks, and implications. *Atmospheric Chemistry and Physics*, 16(4), 1937– 1953. https://doi.org/10.5194/acp-16-1937-2016

Whiting, G. J., & Chanton, J. P. (1993). Primary production control of methane emission from wetlands. *Nature*, 364(6440), 794– 795. https://doi.org/10.1038/364794a0

Woo, M. K., & Guan, X. J. (2006). Hydrological connectivity and seasonal storage change of tundra ponds in a polar oasis environment. *Permafrost and Periglacial Processes*, 17(4), 309– 323. https://doi.org/10.1002/ppp.565

Xu, X. and F. Yuan (2016), Meteorological forcing at Barrow AK 1981–2013. http://ngee-arctic.ornl.gov/. accessed 22 June 2016.

Zhu, X., Zhuang, Q., Gao, X., Sokolov, A., & Schlosser, C. A. (2013). Pan-Arctic land–atmospheric fluxes of methane and carbon dioxide in response to climate change over the 21st century. *Environmental Research Letters*, 8(4), 045003. https://doi.org/10.1088/1748-9326/8/4/045003

Zona, D., Oechel, W., Miller, C. E., Dinardo, S. J., Commane, R., Lindaas, J. O. W., Chang, R. Y.-W., Wofsy, S. C., Sweeney, C., & Karion, A. (2015). *CARVE-ARCSS: Methane Loss from Arctic- fluxes from the Alaskan North Slope*, (pp. 2012– 2014). USA: ORNL DAAC, Oak Ridge, Tennessee. https://doi.org/10.3334/ORNLDAAC/1300